

THE ROOM PRESSURE SPINELLOID PHASES OF THE

NiGa_2O_4 - Ni_2SiO_4 SYSTEM

THE ROOM PRESSURE SPINELLOID PHASES OF THE
 NiGa_2O_4 - Ni_2SiO_4 SYSTEM

by
ROBERT PAUL HAMMOND

A Thesis
Submitted to the School of Graduate Studies
in Partial Fulfillment of the Requirements
for the Degree
Master of Science

McMaster University
August 1991

MASTER OF SCIENCE 1991

McMaster University

Hamilton, Ontario

TITLE: The room pressure spinelloid phases of the NiGa_2O_4 - Ni_2SiO_4 system.

AUTHOR: Robert Paul Hammond, B. Sc. (University of Waterloo)

SUPERVISOR: Dr. Jacques Barbier

NUMBER OF PAGES: ix, 88

ABSTRACT

The ternary oxide system $\text{NiO} - \text{Ga}_2\text{O}_3 - \text{SiO}_2$ has been studied in the temperature range 1400-1550°C at room pressure. Three phases, corresponding to the spinelloid phases I, II, and V, have been identified on the Ni_2GaO_4 (spinel) - Ni_2SiO_4 (olivine) join. These room-pressure phases are isostructural with the high-pressure spinelloid phases of the nickel aluminosilicate system. Single crystals of all three phases have been grown from a silica-rich melt and their crystal structures have been determined by X-ray diffraction. The structure refinements have revealed a strong ordering of the Ga and Si atoms on the tetrahedral sites of all three phases, as well as a clear correlation between spinelloid structure-type and composition. This correlation accounts for the increase in Ni_2SiO_4 content across the series spinel - phase V - phase I - phase II.

ACKNOWLEDGEMENTS

It is said that more than one source is required to make a thesis. It also takes more than one person to create one. I would like first and foremost to thank my supervisor Dr. Jacques Barbier for his assistance with this work.

The single crystal results found in this work were only possible with the assistance of Dr.J. Britten. The technical assistance provided by Mr. J. Garrett and Mr. F. Gibbs was also important in obtaining the results herein. I also thank Dr. J. Reimers for teaching me how to use the wordprocessing package T³, on which this document was prepared.

Finally, I would like to thank my parents for years of assistance and encouragement.

TABLE OF CONTENTS

Chapter		page
1	Introduction	1
2	Diffraction Theory	11
2.1	X-ray Diffraction Theory	11
2.2	Electron Diffraction Theory	19
3	Description of Experiments	24
3.1	Sample Preparation	24
3.1.1	NiGa ₂ O ₄ - Ni ₂ SiO ₄	24
3.1.1.1	Powder Samples	24
3.1.1.2	Single Crystal Samples	25
3.1.2	Other Samples	26
3.1.2.1	Powder Samples	26
3.1.2.2	MgFe ₂ O ₄ - Mg ₂ GeO ₄	26
3.2	Instrumentation	26
3.2.1	Powder X-Ray Diffraction	26
3.2.2	Electron Microscopy	28
3.2.3	Single Crystal Precession Diffraction	29
3.2.4	Single Crystal Diffractometer	29

4	Experimental Results	31
4.1	NiGa ₂ O ₄ - Ni ₂ SiO ₄ Powder Sample Results	31
4.1.1	X-ray Diffraction	32
4.1.2	Electron Diffraction	38
4.2	Single Crystal Results	44
4.2.1	Phase I	45
4.2.2	Phase II	47
4.2.3	Phase V	49
5	Discussion	61
	References	66
	Appendix I Anisotropic temperature factors	71
	Appendix II Observed and calculated structure factors.	73

LIST OF FIGURES

Figure		page
1.1	A schematic pressure - composition diagram of the NiAl_2O_4 - Ni_2SiO_4 system.	2
1.2	The structure of the spinel phase.	4
1.3a	The structure of phase I.	5
1.3b	The structure of phase II.	5
1.3c	The structure of phase III.	6
1.3d	The structure of phase IV.	6
1.3e	The structure of phase V.	7
1.4	The structure of the ω -phase.	7
2.1	The Laue condition for diffraction.	12
2.2	Bragg reflection from a family of lattice planes	14
2.3	The vector f in the complex plane.	16
2.4	A schematic projection of the diffraction pattern formed by the intersection of the Ewald sphere with the reciprocal lattice.	21
3.1	The geometry of the focusing Guinier camera.	27
3.2	Ray diagram for the operating modes of the TEM.	28
3.3	A schematic of a four-circle diffractometer.	30

4.1	The [100] zone axis electron diffraction patterns of the nickel gallosilicate spinelloids.	39
4.2	The [001] zone axis electron diffraction patterns of the nickel gallosilicate spinelloids.	39
4.3	High resolution image of a heavily irradiated spinelloid crystal, showing Moiré fringes.	40
4.4	High resolution image of a phase I crystal with spinel intergrowths.	42
4.5	High resolution image of a phase II crystal with phase I and V intergrowths.	43
4.6	Crystal structure of phase I projected on (100).	53
4.7	Crystal structure of phase II projected on (100).	56
4.8	Crystal structure of phase V projected on (100).	59

LIST OF TABLES

Table		page
4.1	Unit-cell data for the spinelloid phases I, II, and V.	34
4.2	Powder X-ray diffraction pattern for phase I.	35
4.3	Powder X-ray diffraction pattern for phase II.	36
4.4	Powder X-ray diffraction pattern for phase V.	37
4.5	Atomic coordinates, isotropic temperature factors and cation site occupancies for phase I.	51
4.6a	Bond lengths for phase I.	52
4.6b	O-M-O bond angles for phase I.	52
4.7	Atomic coordinates, isotropic temperature factors and cation site occupancies for phase II.	54
4.8a	Bond lengths for phase II.	55
4.8b	O-M-O bond angles for phase II.	55
4.9	Atomic coordinates, isotropic temperature factors and cation site occupancies for phase V.	57
4.10a	Bond lengths for phase V.	58
4.10b	O-M-O bond angles for phase V.	58
4.11	Occupancy and average bond length for the tetrahedral cation sites in the nickel gallosilicate spinelloids	60

CHAPTER 1

INTRODUCTION

The four oxides SiO_2 , MgO , Fe_2O_3 , and Al_2O_3 are thought to be the most abundant oxides in the earth's mantle and olivine, $(\text{Mg}, \text{Fe})_2\text{SiO}_4$, is believed to be the most common mineral in the upper mantle. It is known that at high pressures and temperatures olivine undergoes a phase transformation to the denser spinel structure. The phase relationships of olivine and spinel, and the transformation between the two phases, have been extensively studied (Akimoto et al. 1965, Akimoto and Ida 1966, Akimoto and Fujisawa 1966, 1968, Akimoto and Syono 1970, Dacheville and Roy 1960, Kawai et al. 1966, Ringwood 1956, 1962, 1963, Ringwood and Major, 1966) because of their importance to understanding the geophysical properties of the earth's interior.

In 1970 Ringwood and Major (1970) reported the discovery of a new phase, observed during their study of the $\text{Mg}_2\text{SiO}_4 - \text{Fe}_2\text{SiO}_4$ system. This orthorhombic phase, the β -phase, occurred as an intermediate in the olivine \leftrightarrow spinel transition of synthetic olivines between $(\text{Mg}_{0.8} \text{Fe}_{0.2})_2\text{SiO}_4$ and pure Mg_2SiO_4 . A naturally occurring sample of this phase was later found in a meteorite and was given the name Ringwoodite (Binns et al. 1969). Work by Moore and Smith (1970) has shown that the β -phase crystallized with a modified spinel structure. The same phase was later observed in the Co_2SiO_4 and Mn_2GeO_4 systems (Akimoto and Sato 1968). In 1974 Ma undertook a new type of study (Ma 1974) involving an aluminate (spinel) - orthosilicate (olivine) type join, which used changes in composition to model pressure changes. Ma observed three new orthorhombic phases in the $\text{NiAl}_2\text{O}_4 - \text{Ni}_2\text{SiO}_4$ system, which he named phase I, phase II, and phase III. Ma's work was

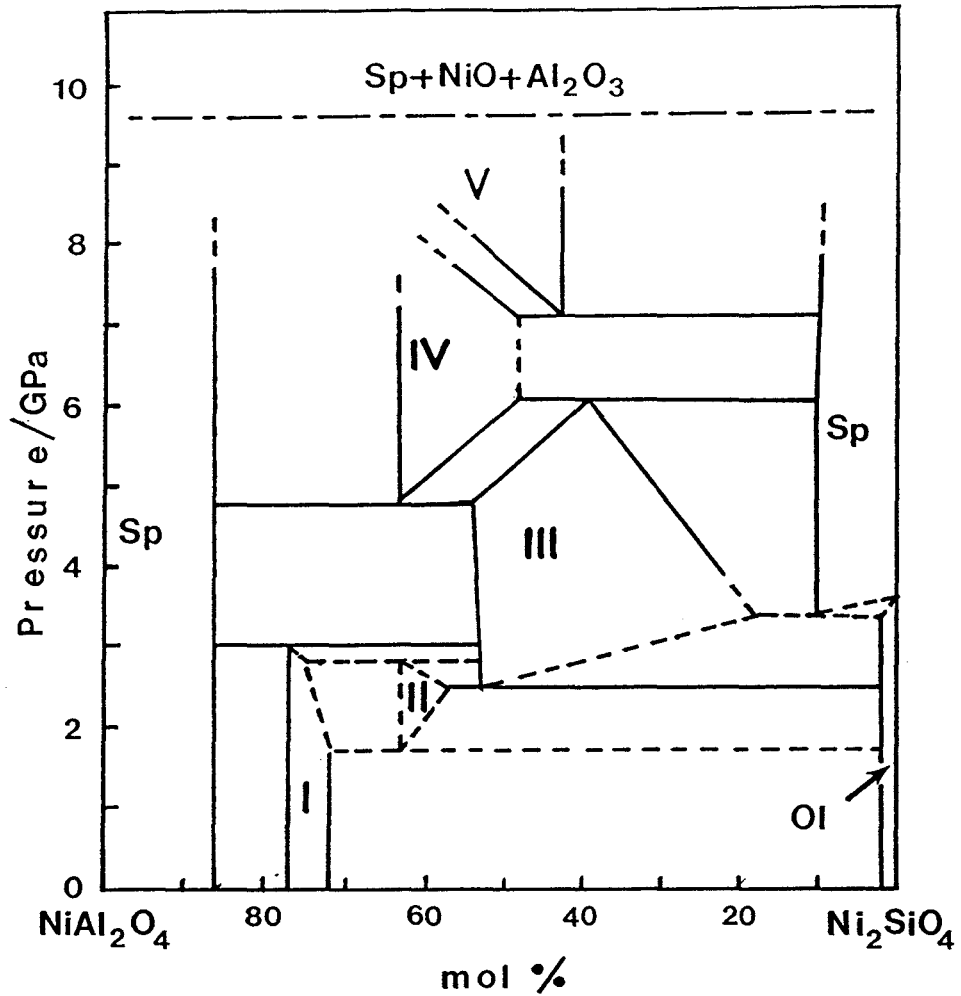


Fig. 1.1 A schematic pressure – composition diagram of the high pressure spinelloid phases in the system $\text{NiAl}_2\text{O}_4 - \text{Ni}_2\text{SiO}_4$ (after Akaogi et al. (1982). Notations are: Sp, spinel; Ol, olivine; I, phase I; II, phase II; III, phase III; IV, phase IV; V, phase V.

extended by Akaogi and his co-workers (1982) who studied the system at higher pressures and discovered two more phases, phase IV and phase V (see Fig. 1.1). They collectively termed these five new phases "spineloids".

The spinelloid phases are considered to be structural derivatives of spinel with compositions lying along the NiAl_2O_4 - Ni_2SiO_4 join, ideally given as $3 \text{NiAl}_2\text{O}_4 : \text{Ni}_2\text{SiO}_4$ for phase I, $3 \text{NiAl}_2\text{O}_4 : 2 \text{Ni}_2\text{SiO}_4$ for phase II, and $\text{NiAl}_2\text{O}_4 : \text{Ni}_2\text{SiO}_4$ for phases III, IV, and V. Phase I is stable between 0.0 to 2.5 GPa (Ma et al. 1975). Phase II was initially reported stable from 2.0 to 2.5 GPa but later work by Akaogi and Navrotsky (1984) and Barbier (1985) has shown that phase II is apparently also stable at room pressure at lower temperatures. Phase II is isostructural with manganostibite (Ma and Tillmans 1975), $\text{Mn}_7\text{SbAsO}_{12}$, a structure related to spinel and first reported by Moore (1970). Phase III is stable between 2.5 and 6.0 GPa and has the same structure as the β -phase of the $(\text{Mg}, \text{Fe})_2\text{SiO}_4$ system (Ma and Sahl 1975). Phases IV and V are stable from 5.0 to 7.2 GPa and 7.0 to 9.5 GPa respectively and both have been described as hybrid structures of spinel and the β -phase (Horioka et al. 1981a, Horioka et al. 1981b). Above 9.5 GPa the spinelloids decompose into Ni_2SiO_4 (spinel), NiO , and Al_2O_3 .

All five phases are orthorhombic with $a \approx 5.66 \text{ \AA}$, $b \approx r \times 2.88 \text{ \AA}$, which is the typical oxygen - oxygen distance for close packing ($r = 4$ (phase I and III), $r = 6$ (phase II), $r = 10$ (phase IV), and $r = 3$ (phase V)), and $c \approx 8.10 \text{ \AA}$. Phases I and V crystallize in the space group $Pmma$, while phases II, III, and IV have $Imma$ symmetry. Hyde et al. (1982) have found a simple, unifying description of the spinelloid phases and described their role in a possible mechanism for the olivine \leftrightarrow spinel transformation. In this scheme, the spinel structure is described using a body centered tetragonal unit-cell, which is half the volume of the conventional cubic unit-cell, and is related to it by $a_t = (a_c + b_c)/2$, $b_t = (-a_c + b_c)/2$, $c_t = c_c$. Fig. 1.2 shows a projection on

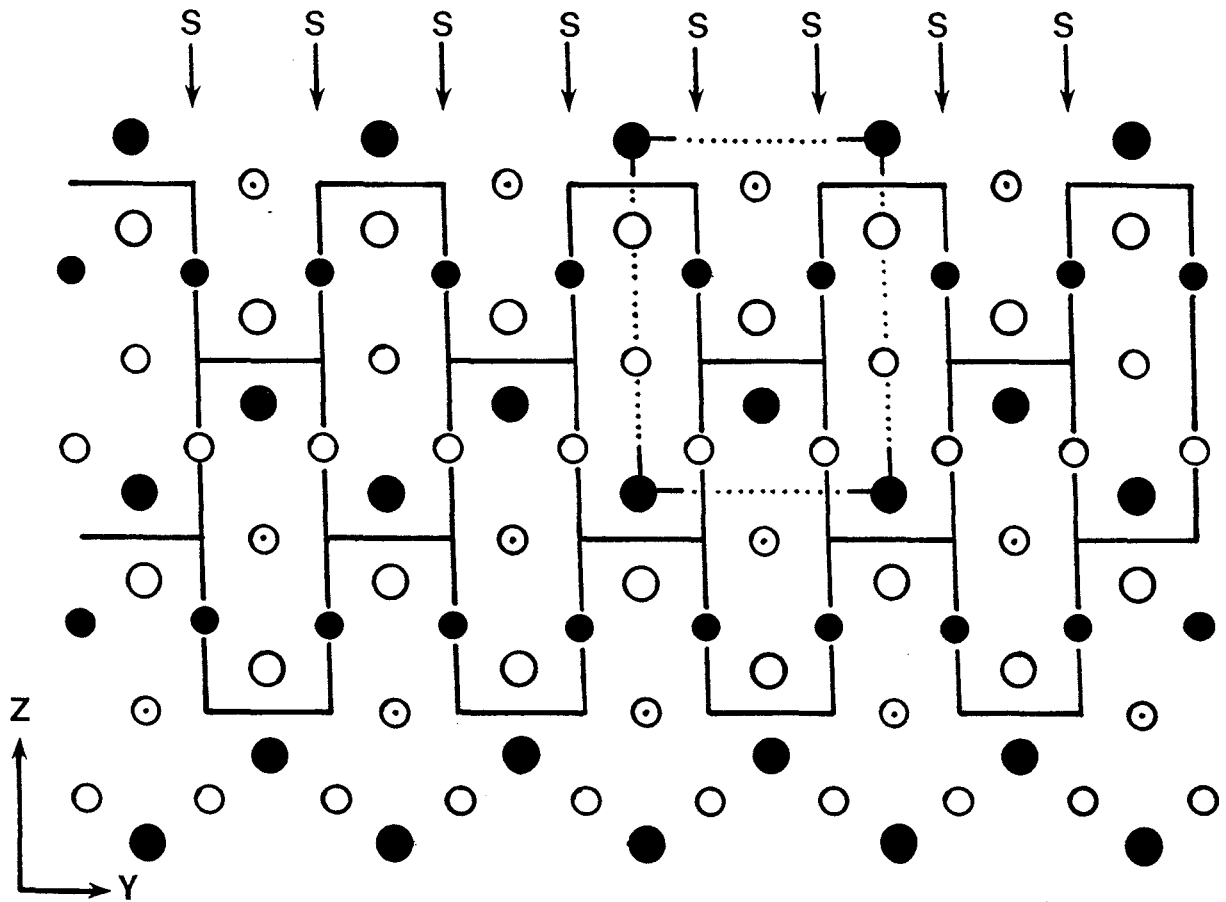


Fig. 1.2 The structure of the spinel phase projected on $(110)_c = (100)_t$ showing only the cations. Large circles are tetrahedrally coordinated cations, small circles are octahedrally coordinated cations, open at $x = \frac{1}{2}$, closed at $x = 0$, and dotted $x = \pm \frac{1}{4}$. The unit cell is shown by the dotted outline. These conventions are also used in Figs 1.3 and 1.4. (Hyde et al. 1982)

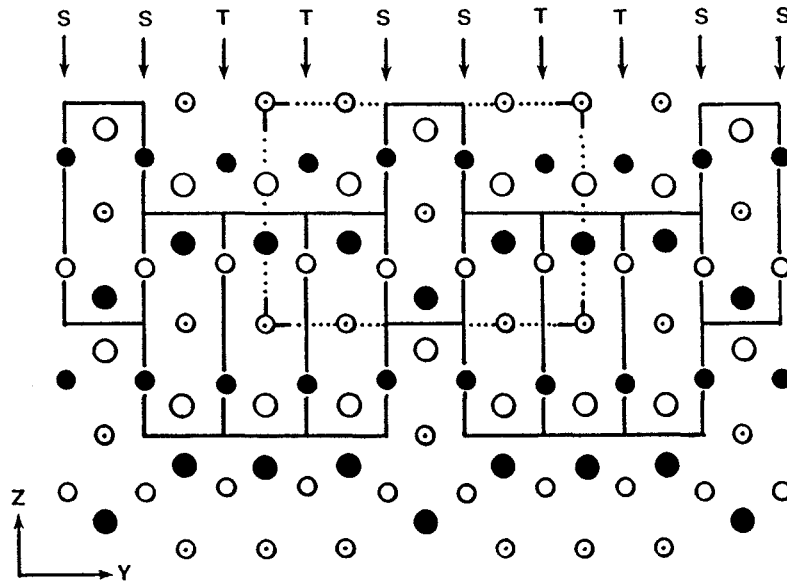


Fig. 1.3a The structure of phase I projected on (100) showing the cations only. (Hyde et al. 1982)

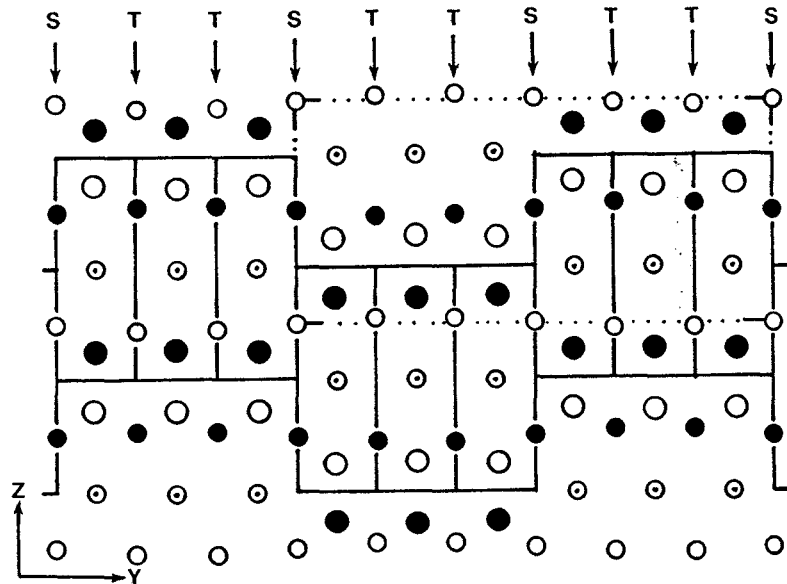


Fig. 1.3b The structure of phase II projected on (100) showing the cations only. (Hyde et al. 1982)

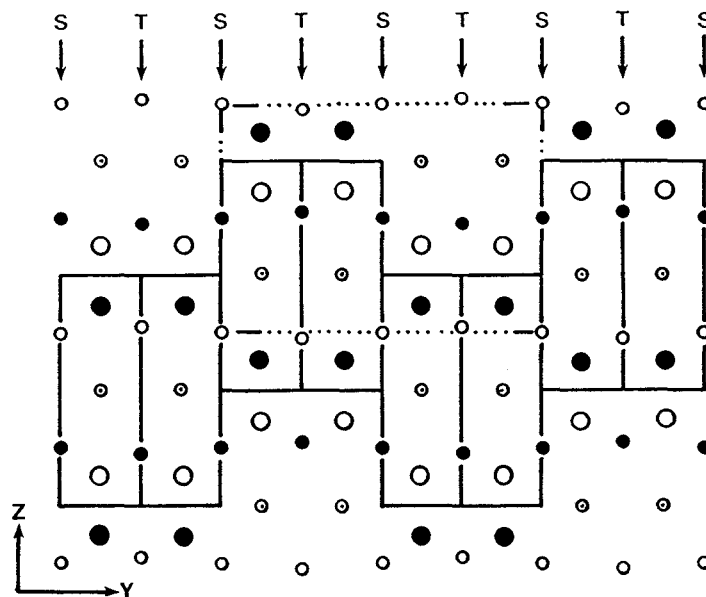


Fig. 1.3c The structure of phase III projected on (100) showing the cations only. (Hyde et al. 1982)

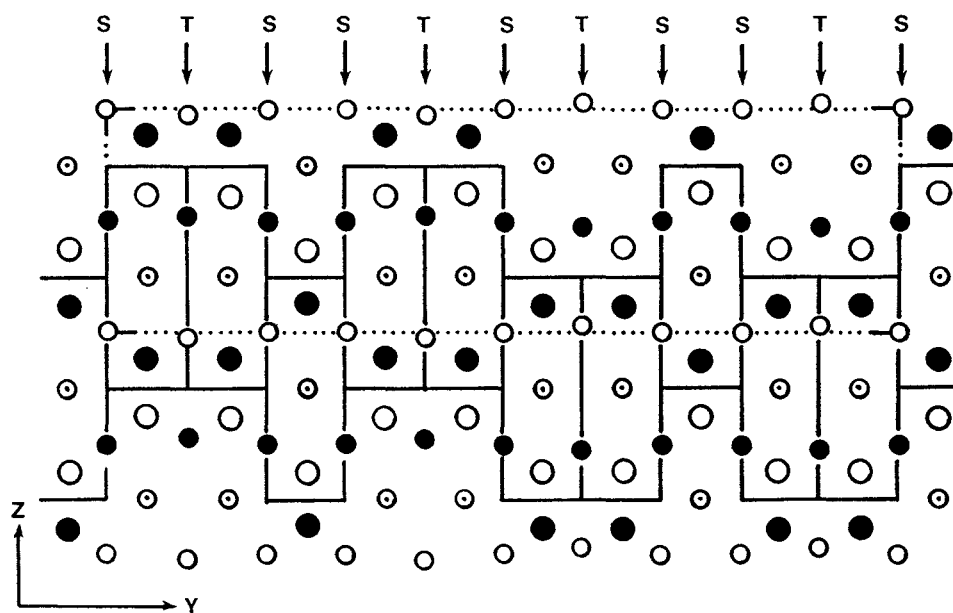


Fig. 1.3d The structure of phase IV projected on (100) showing the cations only. (Hyde et al. 1982)

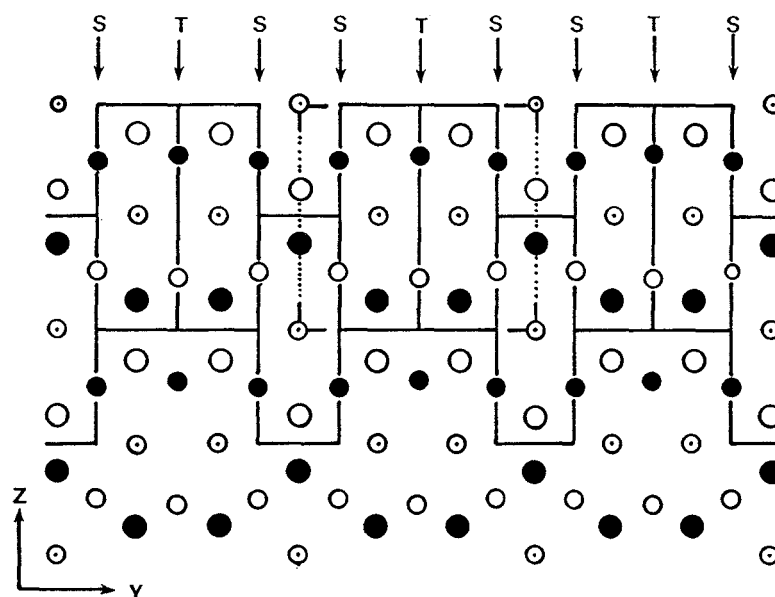


Fig. 1.3e The structure of phase V projected on (100) showing the cations only. (Hyde et al. 1982)

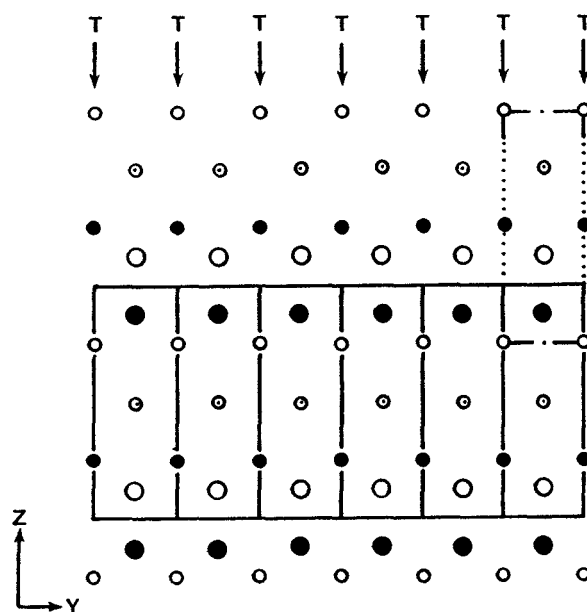


Fig. 1.4 The structure of the ω -phase projected on (100) showing the cations only. (Hyde et al. 1982)

$(100)_t$ of the cation positions in spinel, which can be described as $(010)_t$ slabs of spinel $b_t/2$ thick, separated by anti-phase boundaries (S). The five spinelloid phases are simply derived by replacing some of the S boundaries with reflection/twin planes (T) as shown in Figs. 1.3a-e. Thus the spinelloid phases form a series of structures intermediate between spinel and an unknown ω -phase, obtained by replacement of all the S boundaries with T boundaries as shown in Fig 1.4. Hyde et al. have observed that an $(0\bar{1}2)$ layer of the ω -phase is identical to a single (001) layer, $c/2$ thick, of olivine. The difference between olivine and the ω -phase lay solely in the way in which the layers are joined, resulting in cubic eutaxy of the anions in the ω -phase, and hexagonal eutaxy in the olivine phase. This structural relationship between the two phase allows a simple mechanism for transformation of one phase to the other. One such mechanism, described by Hyde et al., involves a shear of the cation array followed by a shear of the anion array with some small shuffling of the tetrahedral cations in alternate layers to retain proper coordination. Hence a new diffusionless reaction pathway, α -olivine \leftrightarrow ω -phase \leftrightarrow spinelloids \leftrightarrow γ -spinel is proposed for the olivine \leftrightarrow spinel transformation.

The relative stabilities of spinelloid related stacking sequences have been analysed by Price (1983), based on the relative magnitudes of the interaction energies between first, second, and third neighbor structural layers, and it was shown that, of all the polytypic modifications considered, only spinel and the five known spinelloid phases possess a minimum value for the interaction energy between layers. In his energy calculations Price considered two factors, i.e. local electrostatic charge imbalances and ion-size mismatch energy, both resulting from changes in composition across the NiAl_2O_4 - Ni_2SiO_4 system. The former factor is mainly the effect of cation distribution on the charge balance around the oxygen atoms lying on the T - type interface between two structural units. These mirror-related sheets result in one

interfacial oxygen atom being bonded to five octahedral sites and also generate a corner sharing tetrahedral group with another interfacial oxygen atom, bonded to one octahedral and two tetrahedral sites. Such an arrangement is highly unfavorable for Ni_2SiO_4 (with four - coordinated Si^{4+} ions) but becomes more favorable with the introduction of NiAl_2O_4 as NiSi units are replaced with Al_2 , allowing the oxygen atoms to have a better charge balance. At 80% NiAl_2O_4 : 20 % Ni_2SiO_4 a zero-average interaction energy is achieved. The effect of structural mismatch results in a strain energy by causing changes in the relative sizes of the cation coordination polyhedra, thus affecting the packing efficiency of the anion lattice. Price showed that for the aluminosilicate system this effect is minimal and hence he concluded that the stability of the spinelloid phase was primarily due to electrostatic contributions to the interaction energy.

More recently, spinelloid phases were discovered in the MgGa_2O_4 - Mg_2GeO_4 (Barbier and Hyde 1986, Barbier 1989) and MgFe_2O_4 - Mg_2GeO_4 (Barbier 1989) systems. Three spinelloid phases were identified in the MgGa_2O_4 - Mg_2GeO_4 system. $\text{Mg}_3\text{Ga}_2\text{GeO}_8(\text{III})$, isostructural with the spinelloid phase III in NiAl_2O_4 - Ni_2SiO_4 , is stable at room pressure up to 1420°C , above which it decomposes reversibly into spinel and olivine. It also transforms into $\text{Mg}_3\text{Ga}_2\text{GeO}_8(\text{IV})$, isostructural with the spinelloid phase IV, at around 30 kbar at 1100°C . Further increasing the pressure to 60 kbar causes a new phase transition to a mixture of spinel and $\text{Mg}_3\text{Ga}_2\text{GeO}_8(\text{V})$, isostructural with the spinelloid phase V. In the MgFe_2O_4 - Mg_2GeO_4 system only one spinelloid phase, $\text{Mg}_3\text{Fe}_2\text{GeO}_8(\text{III})$, has so far been observed. Like $\text{Mg}_3\text{Ga}_2\text{GeO}_8(\text{III})$, it is stable at room pressure. Several other systems, including MgAl_2O_4 - Mg_2SiO_4 , MnGa_2O_4 - Mn_2GeO_4 , CdGa_2O_4 - CdGe_2O_4 , ZnGa_2O_4 - Zn_2GeO_4 , and NiGa_2O_4 - Ni_2GeO_4 were investigated with negative results (Barbier and Hyde 1986). Based on these observations, these authors suggested that the formation of spinelloid phases at room pressure in spinel - olivine systems, requires that

the spinel end-member has an inverse structure such as NiAl_2O_4 (80% inverse), MgGa_2O_4 (85% inverse), and MgFe_2O_4 (100% inverse).

The purpose of this study was to extend the work done on room - pressure spinelloids by investigating other systems likely to contain such phases. Four systems, each of which contains an inverse spinel end-member were investigated as a part of this work: $\text{NiGa}_2\text{O}_4 - \text{Ni}_2\text{SiO}_4$, $\text{CdGa}_2\text{O}_4 - \text{Cd}_2\text{GeO}_4$, $\text{CoGa}_2\text{O}_4 - \text{Co}_2\text{SiO}_4$, $\text{MgGa}_2\text{O}_4 - \text{Mg}_2\text{SiO}_4$, and $\text{NiFe}_2\text{O}_4 - \text{Ni}_2\text{SiO}_4$. The $\text{MgAl}_2\text{O}_4 - \text{Mg}_2\text{SiO}_4$ and $\text{MgAl}_2\text{O}_4 - \text{Mg}_2\text{GeO}_4$ systems were also investigated, even though MgAl_2O_4 is a normal spinel, to determine if high temperatures were sufficient to prepare room-pressure spinelloids. The work reported in this thesis deals mainly with the $\text{NiGa}_2\text{O}_4 - \text{Ni}_2\text{SiO}_4$ system.

CHAPTER 2

DIFFRACTION THEORY

This chapter will summarize the basic theories of diffraction for X-rays and electrons by crystalline materials. The information for X-ray diffraction is taken from Ashcroft and Mermin (1976 Chapt. 6) and Stout and Jensen (1989 Chapt. 2), while the material on electron diffraction is drawn from Reimer (1984) and Rymer (1970 Chaps. 3 and 6).

2.1 X-ray Diffraction Theory

In 1912 von Laue proposed that X-rays could be diffracted by crystals, and conducted the experiment which confirmed his prediction. Laue regarded a crystal as a three dimensional array of identical objects in a Bravais lattice, each of which could scatter an incident X-ray beam. Although the beam is scattered in all directions, strong intensities of diffracted radiation will be observed in directions and wavelengths for which the rays scattered from each object are in phase, while no intensity is observed where such rays are out of phase.

To determine the conditions under which the rays are scattered coherently, consider two scattering objects separated by vector \mathbf{d} (see Fig. 2.1). An incident beam of parallel X-rays, travelling in direction \mathbf{n} with wavelength λ and wavevector $\mathbf{k} = 2\pi\mathbf{n}/\lambda$ illuminates the objects and is elastically scattered in direction \mathbf{n}' with wavevector $\mathbf{k}' = 2\pi\mathbf{n}'/\lambda$. Constructive interference occurs only if the path difference between the two rays is an integral number of wavelengths. The

condition for constructive interference is thus

$$d \circ (\mathbf{n} - \mathbf{n}') = m\lambda \quad (\text{Fig. 2.1}) \quad [2.1]$$

where m is integral. Multiplying [2.1] by $2\pi/\lambda$ gives the conditions on the incident and scattered wavevectors:

$$d \circ (\mathbf{k} - \mathbf{k}') = 2\pi m \quad [2.2]$$

For an array of scatterers at the sites of a Bravais lattice, displaced from one another by the Bravais lattice vector \mathbf{R} , the condition for coherent scattering is that

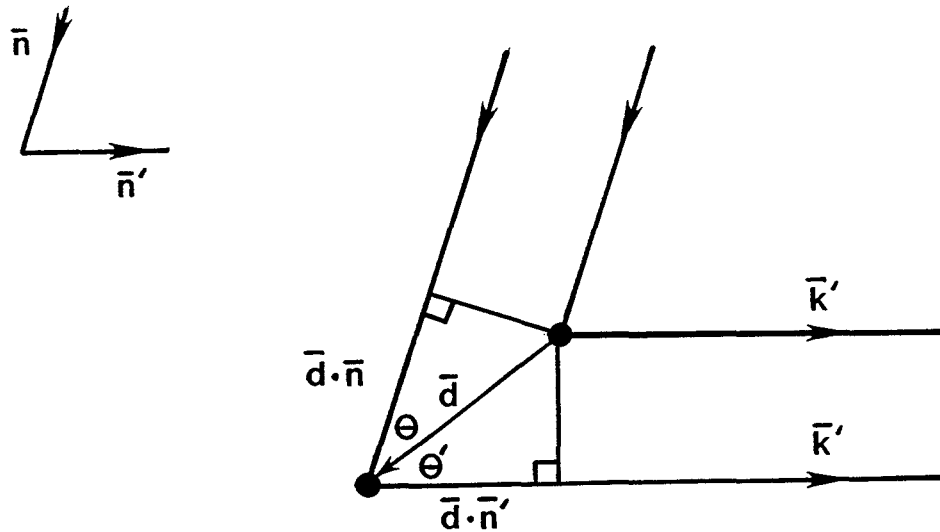


Fig. 2.1 The Laue condition for constructive interference. The path difference between the rays scattered by two atoms is $d \circ (\mathbf{n} - \mathbf{n}')$ where d is the vector separating the two atoms. (Ashcroft and Mermin 1976)

[2.2] holds simultaneously for all values of \mathbf{d} that are Bravais lattice vectors.

$$\mathbf{R} \cdot (\mathbf{k} - \mathbf{k}') = 2\pi m, \quad [2.3]$$

for integral m and all Bravais lattice vectors \mathbf{R} . A reciprocal lattice is defined by the set of all wavevectors \mathbf{K} that will yield plane waves with the periodicity of a given Bravais lattice, leading to the relation:

$$\exp\{i \mathbf{K} \cdot \mathbf{R}\} = 1. \quad [2.4a]$$

Using the relationship $\exp\{n i 2\pi\} = 1$ for integral n , [2.3] can be rewritten in the form:

$$\exp\{i(\mathbf{k} - \mathbf{k}') \cdot \mathbf{R}\} = 1 \quad [2.4b]$$

From a comparison of [2.4a] and [2.4b] it is clear that the Laue condition for constructive interference will occur only if the change in wavevector $\mathbf{k} - \mathbf{k}' = \mathbf{K}$, a vector of the reciprocal lattice.

During the same year von Laue described X-ray diffraction based on a three dimensional lattice, W.L. Bragg observed that diffraction by crystalline materials could be treated as a "refection" of the primary beam from planes in the crystal lattice, and could be described by a simple equation.

To derive the Bragg equation, consider a beam of parallel X-rays, \mathbf{R}_1 and \mathbf{R}_2 , being elastically reflected by a pair of parallel planes P_1 and P_2 with interplanar spacing d (Fig. 2.2). The incident X-rays make an angle θ with these planes. The oscillating electric vector of the X-ray photons will cause electrons, assumed to be at O and C , to vibrate with the same frequency and resulting in them radiating in

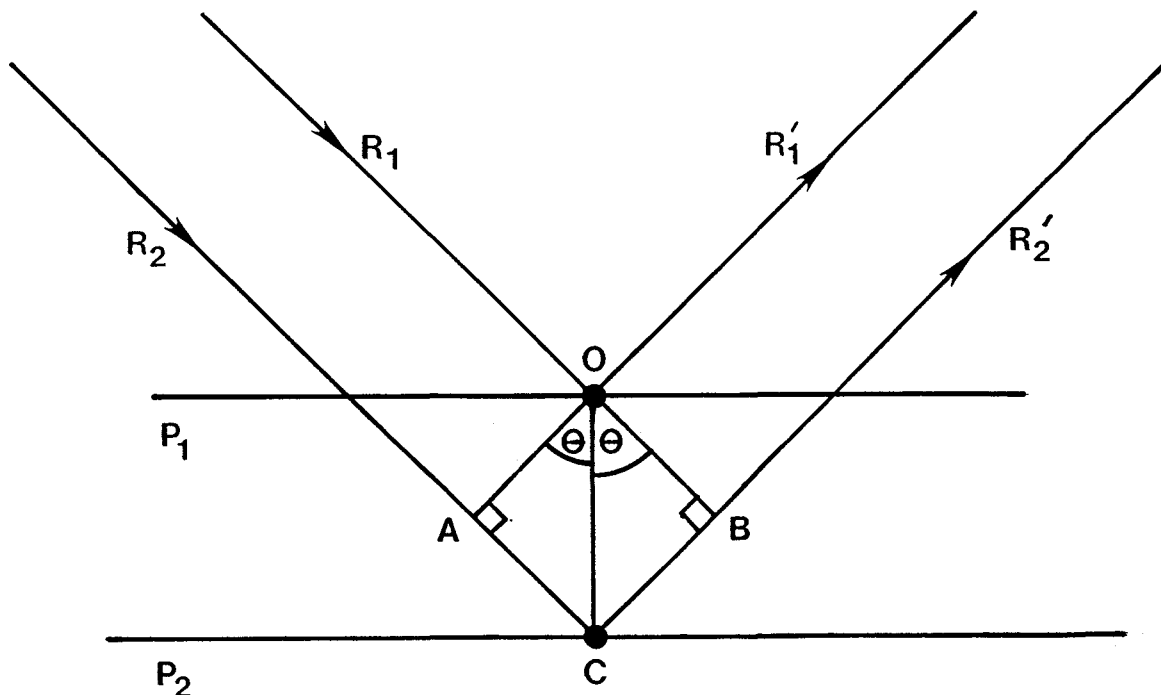


Fig. 2.2 Bragg reflection from a family of lattice planes. The path difference from A to B must equal an integral number of wavelengths. (Stout and Jensen 1989)

all directions. For the particular direction where parallel secondary rays R_1' and R_2' are emitted, at angle θ to the planes, a maximum intensity will be observed if the two rays are in phase. For this to occur, the difference in path length of the rays must be equal to an integral number of wavelengths, λ . Dropping perpendicular lines from O to A and B, it is clear that $AC = BC$. Thus, for the two rays to be in phase

$$2AC = n\lambda \quad [2.5]$$

where n is integral. By definition $AC/d \equiv \sin\theta$ and so simple substitution yields

Bragg's Law:

$$2d \sin \theta = n\lambda \quad [2.6]$$

While the Bragg equation represents the special case of electrons at points O and C, it is a simple exercise of geometry to show that this is also true for the general cases of electrons at any point on, or between, the two planes.

The reciprocal lattice is described by three vectors (\mathbf{a}^* , \mathbf{b}^* , \mathbf{c}^*), which are related to the direct space vectors (\mathbf{a} , \mathbf{b} , \mathbf{c}) of the Bravais lattice, by the relationships:

$$\mathbf{a}^* = \frac{2\pi (\mathbf{b} \times \mathbf{c})}{\mathbf{a} \cdot (\mathbf{b} \times \mathbf{c})} \quad \mathbf{b}^* = \frac{2\pi (\mathbf{c} \times \mathbf{a})}{\mathbf{b} \cdot (\mathbf{c} \times \mathbf{a})} \quad \mathbf{c}^* = \frac{2\pi (\mathbf{a} \times \mathbf{b})}{\mathbf{c} \cdot (\mathbf{a} \times \mathbf{b})} \quad [2.7]$$

Any point on the reciprocal lattice can be described by a reciprocal lattice vector $\mathbf{K} = h\mathbf{a}^* + k\mathbf{b}^* + l\mathbf{c}^*$. If a set of crystal lattice planes are separated by a distance d , then the shortest reciprocal lattice vector normal to the planes will have length $2\pi/d$. The coordinates of this reciprocal lattice vector are known as the Miller indices of the lattice plane. These indices are the reciprocal of the fractional intersection of the unit cell edge by the lattice plane, and so a direct lattice plane described by Miller indices $(h \ k \ l)$ has intercept \mathbf{a}/h , \mathbf{b}/k , and \mathbf{c}/l .

Thus a Laue diffraction peak corresponding to a change in wavevector, $\mathbf{K} = h\mathbf{a}^* + k\mathbf{b}^* + l\mathbf{c}^*$, a reciprocal lattice vector, corresponds to a Bragg reflection from the family of planes $(h \ k \ l)$ perpendicular to \mathbf{K} . While the two treatments explain the same phenomenon and the Laue treatment is more rigorous, it is Bragg's Law that is most commonly used in crystallography.

While the unit-cell dimensions and symmetry will determine the location of the reflections in reciprocal space, it is the arrangement of atoms within the unit-cell that will determine the intensity of each reflection. Each atom in the unit-cell has a scattering factor which is a function of the atom type and $\sin \theta / \lambda$, where θ is the Bragg angle. The scattering power of a particular atom for a given scattering direction is known as its scattering factor f_0 . For $\sin \theta = 0$, $f_0 = Z$, the atomic number of that atom. As the Bragg angle increases, f_0 will decrease, as X-rays being scattered from different points within the electron cloud will be slightly out of phase, causing some destructive interference, a consequence of the finite size of the electron cloud. Thermal motion of the atom will cause an increase in the size of the electron cloud, causing f_0 to diminish even more rapidly. As a consequence the actual scattering factor is not simply f_0 , but rather

$$f = f_0 \exp \{-B \sin^2 \theta / \lambda^2\} \quad [2.8]$$

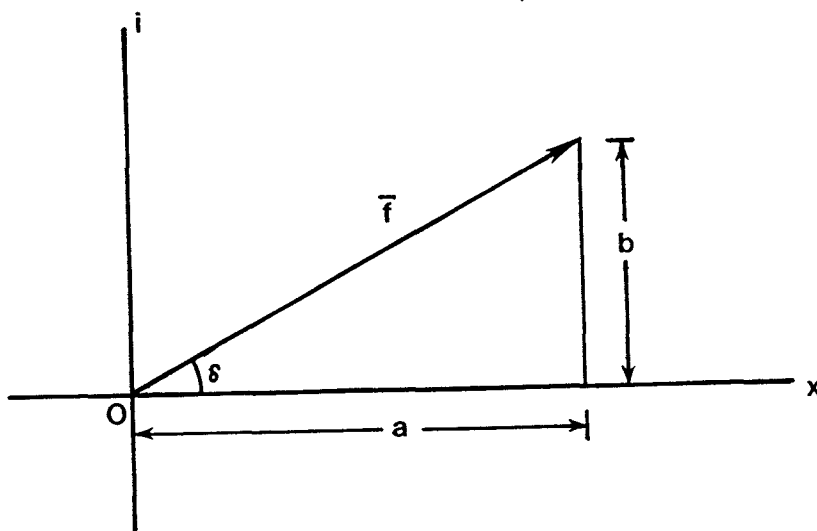


Fig 2.3 The vector f in the complex plane with magnitude $|f|$ at phase angle δ . (Stout and Jensen 1989)

The structure factor F of reflection hkl is defined as the sum of the N waves scattered in the direction of the reflection by the N atoms of the unit-cell, each wave having an amplitude proportional to f_j , the scattering factor for atom j , and a phase δ_j measured with respect to the unit-cell origin. The scattering factor and phase angle can be represented as a vector of length f_j in a complex plane at angle δ_j to the positive real axis (Fig. 2.3). In this form the scattering factor can be expressed as:

$$a + ib = f_j (\cos \delta_j + i \sin \delta_j). \quad [2.9]$$

As a result the structure factor can be found by:

$$F_{hkl} = \sum_j f_j \cos \delta_j + i \sum_j f_j \sin \delta_j. \quad [2.10]$$

Recognizing that the phase difference in radians between the origin and the point (x_j, y_j, z_j) is

$$\delta_j = 2\pi (hx_j + ky_j + lz_j), \quad [2.11]$$

then [2.10] becomes

$$\begin{aligned} F_{hkl} = & \sum_j f_j \cos 2\pi (hx_j + ky_j + lz_j) \\ & + i \sum_j f_j \sin 2\pi (hx_j + ky_j + lz_j). \end{aligned} \quad [2.12]$$

Using the well known relationship

$$\exp \{i\delta\} = \cos \delta + i \sin \delta \quad [2.13]$$

the structure factor can be reduced to

$$F_{hkl} = \sum_j f_j \exp \{2\pi i (hx_j + ky_j + lz_j)\} \quad [2.14]$$

which is the structure factor in exponential form for the hkl reflection.

While [2.14] shows how the structure factor can be obtained from a particular electron distribution, a crystal structure determination requires the reverse, i.e. to obtain the electron density from the structure factors. Using a three dimensional Fourier series, the electron density can be represented by

$$\rho(x, y, z) = \frac{1}{V} \sum_h \sum_k \sum_l F_{hkl} \exp \{-2\pi i(hx + ky + lz)\} \quad [2.15]$$

where V is the volume of the unit-cell.

Note that [2.14] represents the structure factors in terms of the electron density of the unit-cell while [2.15] represents the electron density of the unit-cell based on the structure factors, allowing the conclusion that the structure factors are the Fourier transform of the electron density and that the electron density is the Fourier transform of the structure factors.

Thus, by calculation of the structure factors for each observed reflection, it is possible, via a Fourier synthesis, to obtain the electron density distribution of the unit-cell of a crystal. These structure factors are obtained from a model of the atomic positions within the unit-cell, which is refined by minimizing the function:

$$D = \sum_{hkl} w_r (|F_o| - |k F_c|)^2 \quad [2.16]$$

where w_r is the weight given to the observed reflection, F_o and F_c are the observed and calculated structure factors, and k is a scaling parameter. The overall

agreement between the observed and calculated structure factors is measured by the residual index R , calculated by

$$R = (\Sigma ||F_o| - |F_c| |) / \Sigma |F_o| \quad [2.17]$$

or by using a weighted residual index wR . Setting $\Delta F = |F_o| - |F_c|$.

$$wR = \sqrt{\frac{\Sigma w \cdot |\Delta F|^2}{\Sigma w \cdot |F_o|^2}} \quad [2.18]$$

2.2 Electron Diffraction Theory

According to de Broglie, a particle with momentum p has a wavelength of

$$\lambda = h/p \quad [2.19]$$

where h is Planck's constant. An electron, accelerated through a potential P will have a wavelength

$$\lambda = h / \sqrt{(2 m_o e P)} \quad [2.20]$$

where m_o and e are the rest mass and charge of an electron. If the potential is high enough, then the velocity of the electron approaches c and it is necessary to make relativistic corrections to [2.20] resulting in

$$\lambda = \frac{h}{[2m_o e P (1 + e P / 2m_o c^2)]^{1/2}} \quad [2.21]$$

At 150 eV an electron has a wavelength of about 1\AA , small enough to be used to probe crystal structure by diffraction methods, although much higher energies, typically 100 to 120 keV, are used to improve resolution and penetration while decreasing chromatic aberration. As with X-rays, electrons must satisfy the Laue conditions for diffraction to occur and can also be described using Bragg's Law. At 120 keV $\lambda = 0.0317\text{\AA}$ for an electron and, for a typical interplanar spacing $d_{hkl} = 2\text{\AA}$, the Bragg angle $\theta_B = 0.45^\circ$. Such small angles allow a relaxation of Bragg's law, so that several lattice planes can diffract simultaneously. If the direction of the beam, the zone axis, is $[m\ n\ o]$, then all reflections $(h\ k\ l)$ which satisfy

$$mh + nk + ol = 0 \quad [2.22]$$

are permitted. The small wavelength of the electrons also results in a much larger Ewald sphere, which approximates a plane near the origin of the reciprocal lattice allowing an undistorted view of the reciprocal lattice, as well as circles of reflections from the first and higher Laue zones which are cut by the sphere (see Fig. 2.4). Thus, when using electron diffraction, 2-dimensional sections of the reciprocal lattice of a microscopic single crystal can be observed permitting a visual determination of the reciprocal lattice symmetry, something not possible using powder X-ray techniques.

The intensity of the diffracted beams can be reasonably explained by the kinematic theory, which assumes that each atom receives an incident electron wave of the same intensity. The scattering factor for an electron by an atom is

$$f(\sin \theta / \lambda) = \frac{me^2}{8h^2\pi\epsilon_0} \frac{\lambda^2 (Z - F)}{\sin^2 \theta} \quad [2.23]$$

where Z is the atomic number, F the X-ray scattering factor of the atom, and ϵ_0 is the permittivity of vacuum. Each unit-cell in the crystal is located by the vector

$$\mathbf{r} = m\mathbf{a} + n\mathbf{b} + o\mathbf{c}, \quad [2.24]$$

\mathbf{a} , \mathbf{b} , \mathbf{c} being the vectors defining the three unit-cell axis, and m , n , o being integers.

Each atomic position j within the unit-cell is also defined by the vector

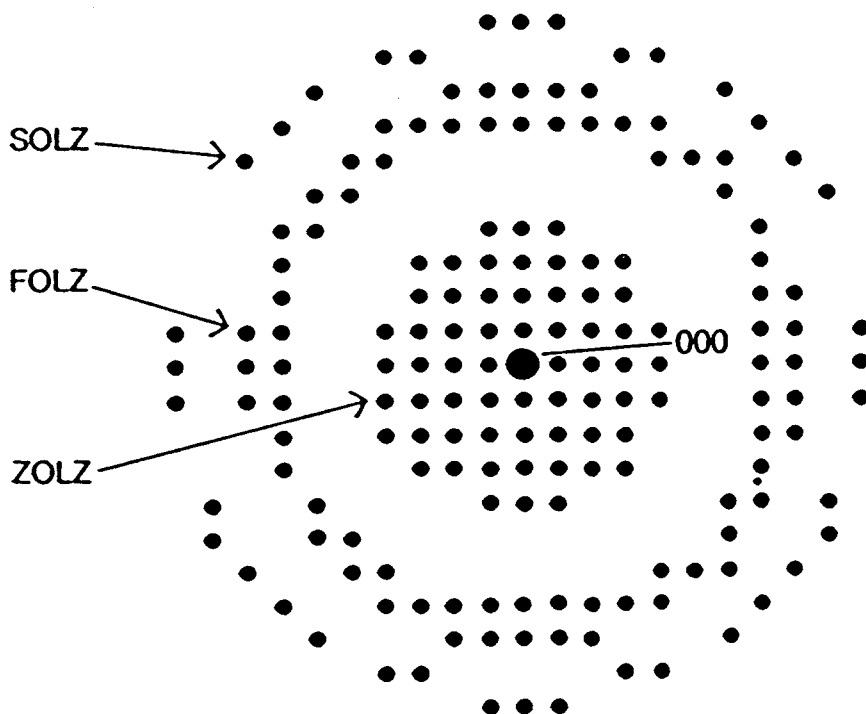


Fig. 2.4 A schematic projection of the diffraction pattern formed by the intersection of the Ewald sphere with the reciprocal lattice at the zero (ZOLZ), first (FOLZ), and second (SOLZ) order Laue zones. (Rymer (1970))

$$\mathbf{r}_j = x_j \mathbf{a} + y_j \mathbf{b} + z_j \mathbf{c} \quad [2.25]$$

where x_j, y_j, z_j are proper fractions. Thus any atom in the crystal is located by the vector

$$\mathbf{R} = (m + x_j) \mathbf{a} + (n + y_j) \mathbf{b} + (o + z_j) \mathbf{c}. \quad [2.26]$$

Since the Laue conditions apply, [2.3] holds and the phase difference between the scattered waves is

$$\phi = \frac{-2\pi}{\lambda} \mathbf{R} \cdot (\mathbf{k}' - \mathbf{k}). \quad [2.27]$$

Thus the total wave scattered by all the atoms of the crystal is

$$\psi = \frac{-\exp \{i\mathbf{K} \cdot \mathbf{R}\}}{r} \sum_{m n o} \sum_j f_j \exp \{2\pi i (\mathbf{k}' - \mathbf{k}) \cdot (\mathbf{r} + \mathbf{r}_j)\} \quad [2.28]$$

which can be rewritten

$$p = \frac{-\exp \{i\mathbf{K} \cdot \mathbf{R}\}}{r} E G$$

where

$$E = \sum_j f_j \exp \{2\pi i (\mathbf{k}' - \mathbf{k}) \cdot (\mathbf{r}_j)\}$$

and

$$G = \sum_{\mathbf{m} \mathbf{n} \mathbf{o}} \exp \{-2\pi i (\mathbf{k}' - \mathbf{k}) \cdot (\mathbf{r})\}$$

The former term is the structure factor and depends solely on the distribution of the unit-cell contents while the latter term is the crystal shape factor and depends upon the size and shape of the crystal. The intensity of the scattered wave is given by

$$I \propto \frac{1}{r^2} |E|^2 |G|^2. \quad [2.29]$$

There are limitations to the kinematic theory, which arise from the initial premise that the primary beam undergoes a negligible intensity loss as it passes through the crystal, resulting in the theory being valid only for thin crystals in which the diffracted intensity is small.

In spite of the elegance of the theory it is not possible to obtain the structure factors from the intensities of the diffracted beams, the strong interactions between the atoms and the electrons result in multiple scattering of the beams, convoluting the intensity data of several reflections into each observed reflection.

CHAPTER 3

DESCRIPTION OF EXPERIMENTS

3.1 Sample Preparation

The following reagents were used for all syntheses:

NiO	(99.99%, Johnson Matthey Chemical Co.)
Ga ₂ O ₃	(99.99%, Aldrich Chemical Co.)
SiO ₂	(99.5%, Johnson Matthey Chemical Co.)
SiO ₂ ·n H ₂ O	(Reagent Grade, Matheson, Coleman, and Bell)
MgO	(99.99%, Aldrich Chemical Co.)
Al ₂ O ₃	(99.99%, Johnson Matthey Chemical Co.)
GeO ₂	(99.999%, Johnson Matthey Chemical Co.)
CdO	(99.0%, Allied Chemical Co.)
CoO	(99.5%, Cerac Inc.)
Fe ₂ O ₃	(99.8%, Baker Chemical Co.)

The water content of the silica gel was determined by thermogravimetric analysis. All reagents were dried for 24 hours at suitable temperatures, and stored in a desiccator.

3.1.1 NiGa₂O₄ – Ni₂SiO₄

3.1.1.1 Powder Samples

All syntheses were originally performed using NiO, Ga₂O₃, and SiO₂ with 1 to 2

wt% of LiF added as a flux because of the slow nature of SiO_2 reactions (Phillips et al. 1963). It was later determined that the LiF interfered with the formation of spinelloid phases in this system and so its use was discontinued, and silica gel was used in place of SiO_2 because it reacted more rapidly.

Samples of 0.4 to 1.0 gram were prepared by mixing the oxides and, where silica gel was used, preheated for 2 hours at 1100°C to dehydrate the gel. The samples were then pelleted and heated in air at 1200°C to 1550°C for periods of 2 to 18 days, with repeated regrinding until no further changes were observed in the powder X-ray diffraction pattern of the reaction products. Partial melting occurred in samples heated to 1550°C .

The products were characterized by powder X-ray diffraction and were further examined by electron diffraction and high resolution electron microscopy.

3.1.1.2 Single Crystal Samples

All syntheses were performed using NiO , Ga_2O_3 , and $\text{SiO}_2 \cdot n \text{H}_2\text{O}$ powders. In all experiments excess silica was used as to provide a flux for crystal growth. Samples of 8 to 10 grams with an excess of 10 to 30 wt% SiO_2 were preheated at 900°C for at least 2 hours to dehydrate the silica. The samples were then heated at 200°C/hr to $1540 - 1600^\circ\text{C}$, soaked for 5 hours, and then slowly cooled at 1° to 2°C/hr to 1550 or 1525°C . The samples were then carefully crushed and the crystals extracted from the flux. It was found that the SiO_2 -rich matrix could be softened by soaking the sample in HF, dissolving the SiO_2 without damaging the crystals, thus allowing easier extraction. The crystals were characterized using a precession camera and the best crystals were then studied using a single crystal diffractometer.

3.1.2 Other Samples

3.1.2.1 Powder Samples

A limited number of samples were prepared from five other spinel – olivine systems ($\text{MgAl}_2\text{O}_4 - \text{Mg}_2\text{GeO}_4$, $\text{CdGa}_2\text{O}_4 - \text{CdGe}_2\text{O}_4$, $\text{CoGa}_2\text{O}_4 - \text{Co}_2\text{SiO}_4$, $\text{MgGa}_2\text{O}_4 - \text{Mg}_2\text{SiO}_4$, and $\text{NiFe}_2\text{O}_4 - \text{Ni}_2\text{SiO}_4$). The 0.4 to 0.5 gram samples were prepared from the oxide powders. The silicate samples were heated in air at temperatures between 1475 – 1600 °C, with the exception of the cobalt samples which could only be heated to 1300° C before melting. Germanate samples were heated in air from 700 – 1100° C, while above 1100° C they were sealed in platinum tubes. The reaction products were characterized by powder X–ray diffraction.

3.1.2.2 $\text{MgFe}_2\text{O}_4 - \text{Mg}_2\text{GeO}_4$ Single Crystals

Efforts were made to prepare single crystals of $\text{Mg}_3\text{Fe}_2\text{GeO}_8(\text{III})$ which had been previously reported by Barbier (1989). A sample of the composition $\text{MgFe}_2\text{O}_4 : \text{Mg}_2\text{GeO}_4$ was prepared from the oxides with a further 20 wt% excess of GeO_2 added. This sample did not melt below 1200° C. New samples were prepared using MgF_2 as a flux instead of excess GeO_2 . Pre–reacted samples of $\text{Mg}_3\text{Fe}_2\text{GeO}_8(\text{III})$ with 10 to 50 wt% added MgF_2 were heated for 1 to 4 days at 1300° to 1400° C. Some recrystallization did take place but no crystals of sufficient size for single crystal experiments could be obtained.

3.2 Instrumentation

3.2.1 Powder X–ray Diffraction

All powder X–ray diffraction was performed using a Guinier – Hägg focusing camera ($\lambda \text{ Cu K}\alpha_1 = 1.54056 \text{ \AA}$). The camera contains a large single crystal quartz

monochromator oriented so that one set of strongly diffracting planes is at the Bragg angle to the incident beam. The Bragg angle is set so that only the $\text{Cu K}\alpha_1$ rays are diffracted, giving a monochromatic beam. The crystal is also bent so that the divergent incident beam is diffracted into a convergent beam focused onto the diffraction circle, which holds a piece of film. The geometry of the camera is shown in Fig. 3.1. The monochromatic radiation passes through the sample at X. Radiation which is not diffracted by the sample will focus on a beam stop at A while diffracted beams will focus on the circle at B, C, etc. where their position is recorded by the film. The beam stop is briefly removed to allow a reference line at $2\theta = 0$ to be recorded. The positions and intensities of the lines were then measured using a KEJ LS-20 computer controlled digital line scanner. The unit-cell dimensions were determined from the powder data using the computer software program LSUDF.

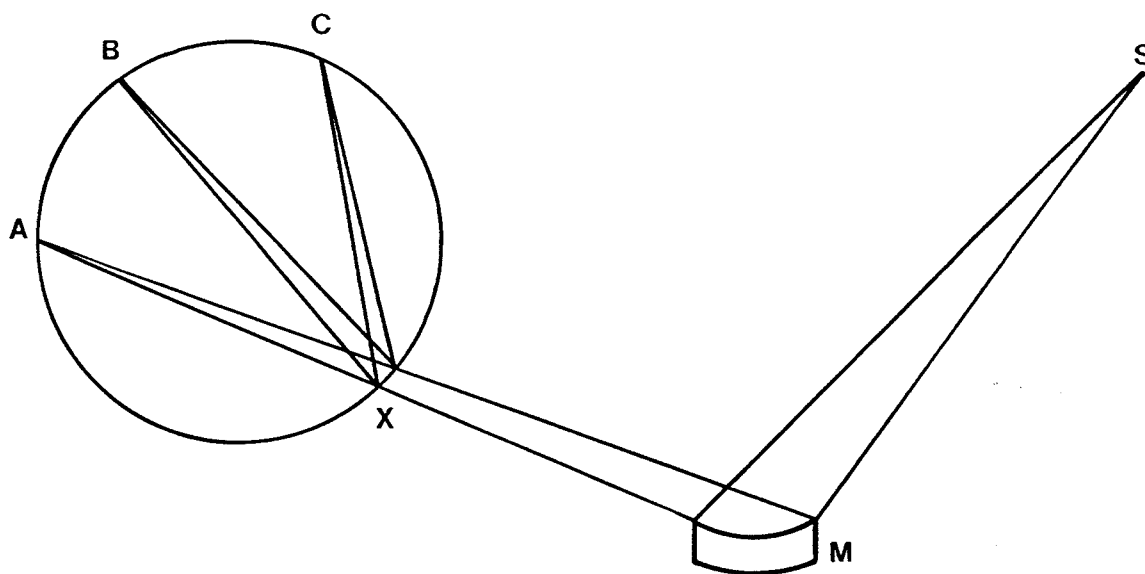


Fig. 3.1 The geometry of the focusing Guinier camera. (West 1989)

3.2.2 Electron Microscopy

A Philips CM-12 transmission electron microscope (TEM) operating at 120 keV was used to examine microscopic single crystals in the powder samples. The TEM was operated in the bright field imaging (BF) and selected area electron diffraction (SAED) modes. A ray diagram in comparing these modes is shown in Fig. 3.2. In the BF mode the intermediate lens

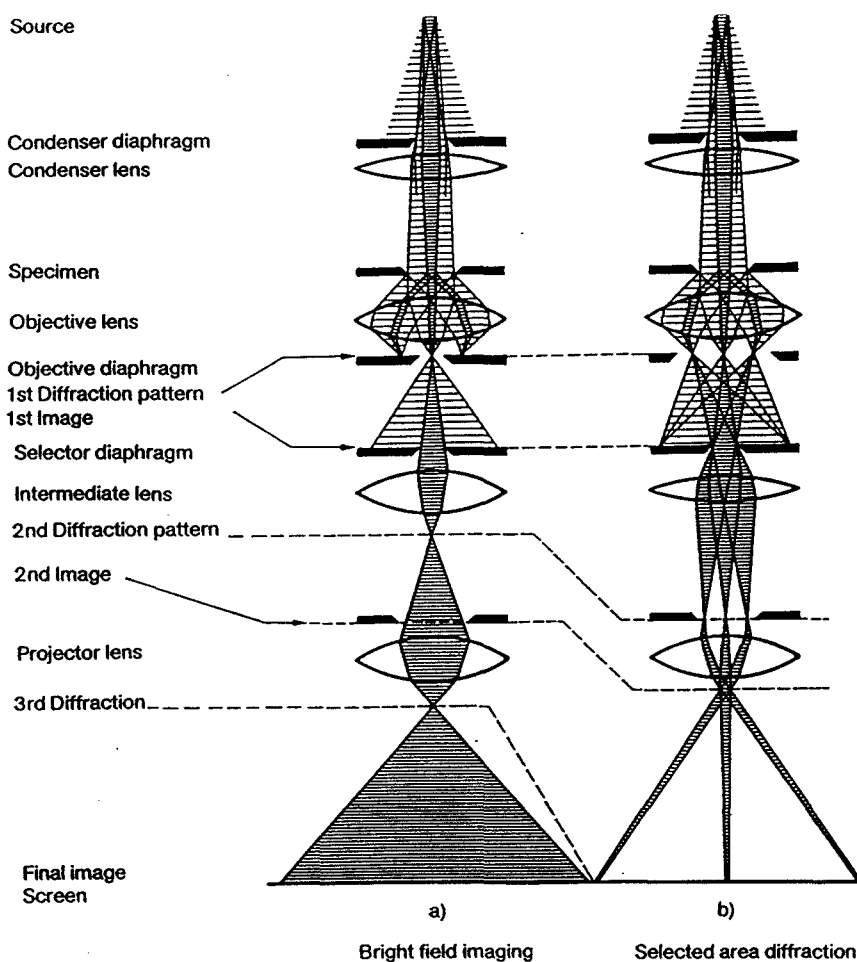


Fig. 3.2 Ray diagram for a transmission electron microscope in a) the imaging and b) selected area diffraction (SAED) modes. (Reimer 1984)

is focused on the image plane of the objective lens, whereas during an SAED experiment it is focused on the back focal plane of the objective lens. When an SAED aperture is in place, the SAED pattern will directly correspond to the material in the region being imaged in the BF mode.

3.2.3 Single Crystal Precession Photographs

Single crystal precession photographs (λ Mo $K\alpha = 0.71069 \text{ \AA}$) were taken to determine the nature and quality of spinelloid single crystals obtained from the flux-growth experiments. Each crystal was mounted on a glass fiber using nail polish as an adhesive. The fiber was mounted on a goniometer and aligned on the camera so that one cell - axis was parallel to the beam. This axis was then offset by an angle μ and precessed about the beam. By keeping a piece of film tangential to the sphere of reflection of the moving crystal, the precession camera allows undistorted images of the reciprocal lattice to be obtained. Photographs of two zero-layers and a first layer containing the b^* -axis (i.e. $[hk1]$ or $[1kl]$) were taken for candidate crystals. It was important to have the b^* -axis in the photographs because it is the only characteristic axis in these phases (c.f. -Table 4.1). Crystals of each phase were identified and one crystal of highest quality was selected from each phase for measurement on the single crystal diffractometer.

3.2.4 Single Crystal Diffractometer Data Collection

The single crystal diffractometer data sets were collected on a Syntex P2₁ diffractometer (λ Ag $K\alpha = 0.56086 \text{ \AA}$) using the Seimens P3/V Data Collection System. The beam was monochromatated by diffracting it off of a highly oriented graphite crystal. Four independent arcs, ϕ , χ , ω , and 2θ (see Fig. 3.3) were used to bring any desired plane into a diffracting position. A detector mounted on the 2θ arc measures the intensity of each reflection, allowing a quantitative determination of the atomic positions within the

unit-cell as outlined in Chapter 2. The structure for each crystal was refined by obtaining an initial solution via direct methods. This initial model was then used to locate all of the oxygen and cation positions in the lattice and to determine approximate temperature factors for each site. To prevent strong correlations in the matrix, the temperature factors were fixed before the silicon/gallium occupancies of the tetrahedral sites were allowed to vary. After obtaining an approximate cation distribution for these sites, the occupancies were again fixed and the temperature factors then allowed to vary. This iteration was repeated until no significant changes occurred, at which point the occupancies were fixed. The cation distributions of the octahedral sites were then calculated and input into the model (see Chapter 4.2) and once again a process of alternately fixing and refining the occupancies and temperature factors was undertaken. A final set of refinements, using anisotropic temperature factors, was then performed.

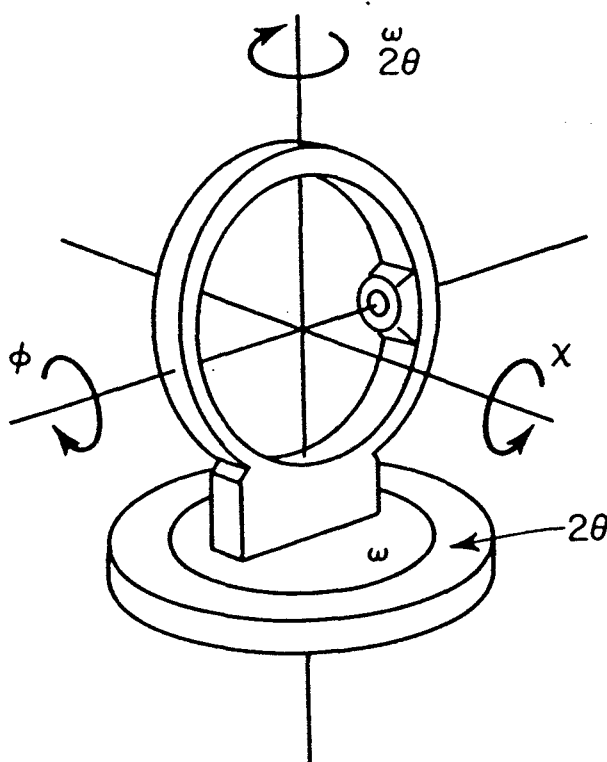


Fig. 3.3 A schematic of a four-circle diffractometer. (Stout and Jensen 1989)

CHAPTER 4

EXPERIMENTAL RESULTS

Of the six systems examined only the $\text{NiGa}_2\text{O}_4 - \text{Ni}_2\text{SiO}_4$ system formed spinelloid phases at room pressure. All other systems contained only spinel, olivine, and starting oxides in the reaction products, with the exception of the $\text{CdGa}_2\text{O}_4 - \text{Cd}_2\text{GeO}_4$ reaction, which also formed the garnet phase, $\text{Cd}_3\text{Ga}_2\text{Ge}_3\text{O}_{12}$. These systems will not be further discussed in this work.

4.1 Powder Sample Results

A survey of the ternary oxide system $\text{NiO}-\text{Ga}_2\text{O}_3-\text{SiO}_2$ was conducted over the temperature range 1200°C to 1550°C at 1 atm pressure. Three previously unknown phases, identified as spinelloid phases I, II, and V, were found, and these were the only ternary phases observed in the system. All of the reaction products contained small amounts of NiO and/or SiO_2 . The presence of these phases was probably a result of slow kinetics or of the decomposition of Ni_2SiO_4 olivine at temperatures above 1400°C (Phillips et al. 1963).

The spinelloids were found for compositions lying on the $\text{NiGa}_2\text{O}_4-\text{Ni}_2\text{SiO}_4$ pseudo-binary join. Our study focused on the ideal compositions of phase I (3 NiGa_2O_4 : 1 Ni_2SiO_4 - Ma et al. 1975), phase II (3 NiGa_2O_4 : 2 Ni_2SiO_4 - Ma 1972), and phase V (NiGa_2O_4 : Ni_2SiO_4 - Horioka et al. 1981b). At temperatures of 1400 to 1450°C , the gallium-rich 3:1 composition contained mostly spinel whereas, in the initial stages of the reaction, the more silica-rich 7:5 and 1:1

compositions yielded mixtures of spinel and phase II. After prolonged heating (8 days or more), these initial products reacted further, first into a mixture of phases I and V, and eventually phase I alone. A similar phase V \rightarrow I transformation was observed in samples sintered directly at 1475 to 1525°C, but with no phase II observed in the initial products. Later experiments showed that after 2 hours at 1475°C samples contained large amounts of phase II, but evidence of phase I formation was already apparent from the powder x-ray patterns. At 1550°C, the 3:1 and partially melted 7:5 compositions contained only spinel, while the partially melted 1:1 composition contained only phase V.

It is therefore clear that, in the nickel gallosilicate system, phase V is stable above 1550°C while phase I is stable between 1400 – 1525°C, and that phase II is stable only at lower temperatures. The appearance of phase V as an intermediate phase at 1400 – 1525°C may be a result of the sluggish reaction rates of silicates: with a poorer silicon content than phase I (see section 4.2), phase V would form first as the spinel phase initially present in the sample begins to react with the nickel oxide and silica. Thus the transitional phase V observed below 1550°C would arise from kinetic, rather than thermodynamic, effects.

4.1.1 X-Ray Diffraction

The powder X-ray diffraction patterns of phases I, II, and V were indexed using an automatic indexing program written by Visser (1969). The non-extinction conditions were consistent with the space groups *Pmma* (phases I and V) and *Imma* (phase II) as determined earlier for the spinelloid phases of the NiAl_2O_4 – Ni_2SiO_4 system. The unit-cell parameters are given in Table 4.1 together with those for the nickel aluminosilicate phases (Ma et al. 1975, Ma and Tillmans 1975, Horioka et al. 1981b). The axial ratios are virtually identical for both series of phases indicating identical small distortions from ideal cubic close packing. As expected from the

longer Ga-O bond, Ga substitution for Al results in larger cell parameters with an isotropic volume increase of approximately 6% for all three phases.

The intensities of the powder X-ray diffraction lines were measured using a computer - controlled KEJ LS-20 line scanner. The intensities were also calculated using the program "Lazy Pulverix" (Yvon et al. 1977) and the previously published atomic positions and cation distributions of the nickel aluminosilicate phases (Ma et al. 1975, Ma and Tillmans 1975, Horioka et al. 1981b). These calculated intensities show a reasonably good agreement with the observed intensities (Tables 4.2, 4.3, 4.4) thus supporting the isotopy of the gallium and aluminum phases. This isotopy was later confirmed from the single crystal results (c.f. section 4.2) which were then used in a second set of calculations, also presented in Tables 4.2 - 4.4. This second set of calculated intensities is very similar to the first, thus the discrepancies between the calculated and observed values may be due to a preferred orientation of the powder sample rather than cation distributions.

Table 4.1: Unit-cell data for spinelloid phases I, II, and V in the $\text{NiX}_2\text{O}_4 - \text{Ni}_2\text{SiO}_4$ (X=Al, Ga) systems.

Phase	Cell Parameters (Å)		
	a	b	c
I(X=Al) ¹	5.6664(5)	11.496(2)	8.093(7)
I(X=Ga) ⁴	5.7743(5)	11.7152(9)	8.2364(6)
II(X=Al) ²	5.6603(7)	17.298(2)	8.110(1)
II(X=Ga) ⁴	5.765(1)	17.619(3)	8.238(2)
V(X=Al) ³	5.665(1)	8.590(1)	8.097(3)
V(X=Ga) ⁴	5.7914(4)	8.7809(7)	8.2346(6)

¹ Ma et al., 1975

² Ma and Tillmans, 1975

³ Horioka et al. 1982b

⁴ powder data for the gallosilicate phases

Table 4.2: Powder X-ray diffraction pattern of phase I nickel gallosilicate (*Pmma*, cell parameters in Table 4.1). Observed intensities were measured using a KEJ LS-20 line scanner. Calculated intensities are based on the aluminosilicate data for I_{cal1} and on single crystal gallosilicate data (cf. Section 4.2) for I_{cal2} .

hkl	d_{cal}	d_{obs}	I_{cal1}	I_{cal2}	I_{obs}
0 0 1	8.236	8.217	65	66	51
1 0 1	4.728	4.726	854	1000	207
1 0 2	3.3528	3.3533	61	102	56
1 1 2	3.2234	3.2235	175	144	118
0 4 0	2.9288	3.9285	132	125	170
1 2 2	2.9099	2.9101	37	41	185
2 0 0	2.8872	2.8872	138	132	145
0 4 1	2.7595	2.7595	27	28	35
0 0 3	2.7455	2.7456	149	140	147
2 0 1	2.7246	2.7249	177	166	182
0 1 3	2.6730	2.6735	233	213	228
1 3 2	2.5438	2.5438	102	80	134
1 4 1	2.4898	2.4894	506	433	858
0 2 3	2.4860		140	161	
1 0 3	2.4795	2.4794	228	200	316
2 2 1	2.4704	2.4706	274	305	239
0 4 2	2.3868	2.3870	140	135	128
2 0 2	2.3640	2.3642	174	166	165
0 3 3	2.2459	2.2457	81	72	84
2 3 1	2.2345	2.2343	192	177	192
1 4 2	2.2058	2.2055	23	43	113
0 0 4	2.0591	2.0574	205	206	750
2 4 0	2.0561		456	459	
0 4 3	2.0030	2.0027	48	43	65
2 4 1	1.9949	1.9950	100	91	128
3 0 1	1.8743	1.8734	56	66	34
0 5 3	1.7822	1.7831	28	24	43
2 5 1	1.7765	1.7768	69	62	104
3 1 2	1.7247	1.7252	27	23	35
1 6 2	1.6873	1.6873	7	7	54
0 4 4	1.6845	1.6848	41	39	79
2 0 4	1.6764	1.6764	64	62	102
3 2 2	1.6712	1.6709	8	8	54
0 1 5	1.6312	1.6306	17	15	47
1 4 4	1.6171	1.6162	19	17	42
0 6 3	1.5912	1.5916	27	31	135
0 2 5	1.5858	1.5861	44	47	231
1 0 5	1.5841	1.5843	58	47	156
3 4 1	1.5787	1.5786	138	119	527
0 3 5	1.5178	1.5177	46	45	77
1 7 2	1.4974	1.4973	9	6	50
0 8 0	1.4644	1.4644	268	262	366
2 4 4	1.4550	1.4549	1000	979	1000
4 0 0	1.4436	1.4437	264	258	343

Table 4.3: Powder X-ray diffraction pattern of phase II nickel gallosilicate (*Imma*, cell parameters in Table 4.1). Observed intensities were measured using a KEJ LS-20 line scanner. Calculated intensities are based on the aluminosilicate data for I_{cal1} and on single crystal gallosilicate data (cf. Section 4.2) for I_{cal2} .

hkl	d_{cal}	d_{obs}	I_{cal1}	I_{cal2}	I_{obs}
1 1 2	3.292	3.295	203	188	40
0 6 0	2.9364	2.9361	111	107	150
1 3 2	2.9109	2.9104	47	99	74
2 0 0	2.8826	2.8847	107	122	282
0 1 3	2.7133	2.7133	452	404	211
2 1 1	2.6889	2.6893	600	571	155
1 6 1	2.4938	2.4959	1000	1000	1000
1 0 3	2.4791	2.4791	396	419	231
0 6 2	2.3911	2.3901	123	121	101
2 0 2	2.3617	2.3610	163	152	157
0 5 3	2.1660	2.1672	110	95	38
2 5 1	2.1535	2.1534	252	243	43
0 0 4	2.0587	2.0573	210	197	681
2 6 0	2.0571		479	452	
0 7 3	1.8555	1.8551	55	54	35
2 7 1	1.8476	1.8484	126	117	58
3 1 2	1.7330	1.7340	30	28	6
2 5 3	1.7316	1.7325	16	14	5
2 0 4	1.6757	1.6758	61	56	74
1 0 5	1.5842	1.5837	121	126	300
3 6 1	1.5782	1.5787	252	269	407
3 5 2	1.5612	1.5609	52	50	8
1 7 4	1.5363	1.5350	27	22	7
0 5 5	1.4925	1.4922	73	68	32
0 12 0	1.4682	1.4678	252	247	231
2 6 4	1.4554	1.4548	920	908	862
1 11 2	1.4452	1.4445	31	31	179
4 0 0	1.4413	1.4419	246	240	199

Table 4.4: Powder X-ray diffraction pattern of phase V nickel gallosilicate (*Pmma*, cell parameters in Table 4.1). Observed intensities were measured using a KEJ LS-20 line scanner. Calculated intensities are based on the aluminosilicate data for I_{cal1} and on single crystal gallosilicate data (cf. Section 4.2) for I_{cal2} .

hkl	d_{cal}	d_{obs}	I_{cal1}	I_{cal2}	I_{obs}
0 1 1	6.000	6.001	111	54	27
1 0 1	4.7326	4.7333	170	90	79
0 3 0	2.9228	2.9233	104	120	116
2 0 0	2.8929	2.8924	103	133	114
0 0 3	2.7424	2.7443	71	51	65
2 0 1	2.7291	2.7297	82	63	45
1 2 2	2.6632	2.6630	201	258	225
0 1 3	2.6174	2.6170	332	309	301
2 1 1	2.6058	2.6054	535	517	284
1 3 1	2.4868	2.4783	1000	1000	1000
1 0 3	2.4781	2.4783	430	438	238
0 3 2	2.3826	2.3830	132	128	114
2 0 2	2.3663	2.3663	154	140	161
0 2 3	2.3250	2.3239	143	150	125
2 2 1	2.3169	2.3164	341	330	196
1 3 2	2.2031	2.2033	29	20	27
0 0 4	2.0568	2.0564	245	174	619
2 3 0	2.0561		532	377	
2 3 1	1.9947	1.9949	42	33	31
1 4 2	1.8347	1.8347	42	52	33
0 4 3	1.7123	1.7116	46	41	63
2 4 1	1.7090	1.7092	104	119	77
0 3 4	1.6821	1.6820	32	46	49
2 0 4	1.6763	1.6763	50	55	55
3 2 2	1.6223	1.6219	48	61	68
0 1 5	1.6172	1.6176	31	36	30
1 0 5	1.5827	1.5823	118	123	191
3 3 1	1.5798	1.5794	243	248	361
3 0 3	1.5776		111	116	
1 5 2	1.5539	1.5544	34	46	23
0 2 5	1.5405	1.5405	74	79	73
0 6 0	1.4614	1.4611	256	237	211
2 3 4	1.4541	1.4541	970	910	831
4 0 0	1.4464	1.4461	253	234	254
3 4 2	1.3658	1.3663	18	22	60

4.1.2 Electron Diffraction

By using electron diffraction on microscopic single crystals, patterns for the [001] and [100] zones of each of the three spinelloid phases were obtained (Figs. 4.1 and 4.2), confirming the unit – cell dimensions determined by powder X–ray diffraction. The [001] orientation shows the systematic absences resulting from the a –glide in all three phases, giving similar patterns for phases II and V (due to the extinctions from the I –centring of phase II and the fact that $b_{II} \approx 2b_V$ –cf. Table 4.1). However very weak extra reflections of the type $\{1k0\}$ were observed in the [001] patterns of the flux–grown samples of phases II and V (Fig. 4.2c). The presence of an a –glide requires that $h=2n$ for $hk0$ reflections, and so any combination of allowed reflections (i.e. double diffraction) will still result in $h=2n$. Thus the observed extra reflections are primary reflections and indicate a loss of the a –glide symmetry. Since these extra reflections were not present in the patterns of sintered samples quenched from high temperature, the associated loss of symmetry may be the result of atomic ordering (probably Ga^{3+}/Si^{4+} on tetrahedral sites) taking place during the slow crystallization process. However, the very weak intensity of these forbidden reflections (undetected on Guinier and precession film patterns) indicates that the structures of the gallosilicate spinelloid phases do not deviate much from the $Pmma$ and $Imma$ symmetries. This was confirmed by the single crystal analyses.

4.1.3 Electron Microscopy

High resolution electron microscopy was used to obtain lattice images of the spinelloid structures. All of the products showed evidence of decomposition in the electron beam, accompanied by the formation of small crystallites. Fig. 4.3

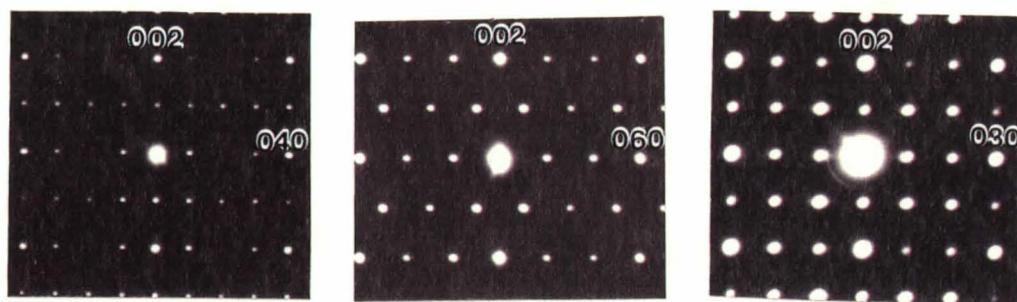


Fig. 4.1 [100] zone axis electron diffraction patterns of nickel gallosilicate: (a) phase I, (b) phase II, (c) phase V. The observed patterns are consistent with the *Pmma* space group for phases I and V and the *Imma* space group for phase II.

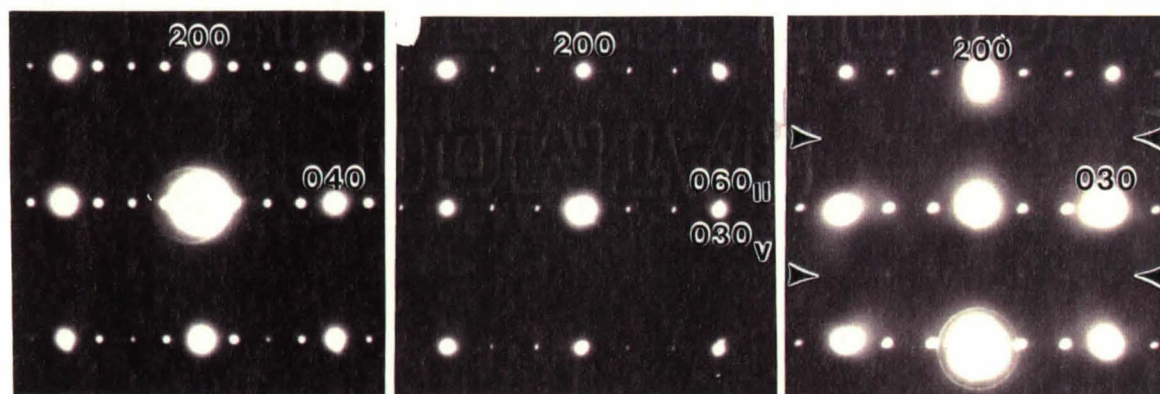


Fig. 4.2 [001] zone axis electron diffraction patterns of nickel gallosilicates: (a) phase I, (b) phase II, (c) phase V. The sample of the flux-grown phase V crystal in (c) shows extra rows of reflections in violation of the *a*-glide.

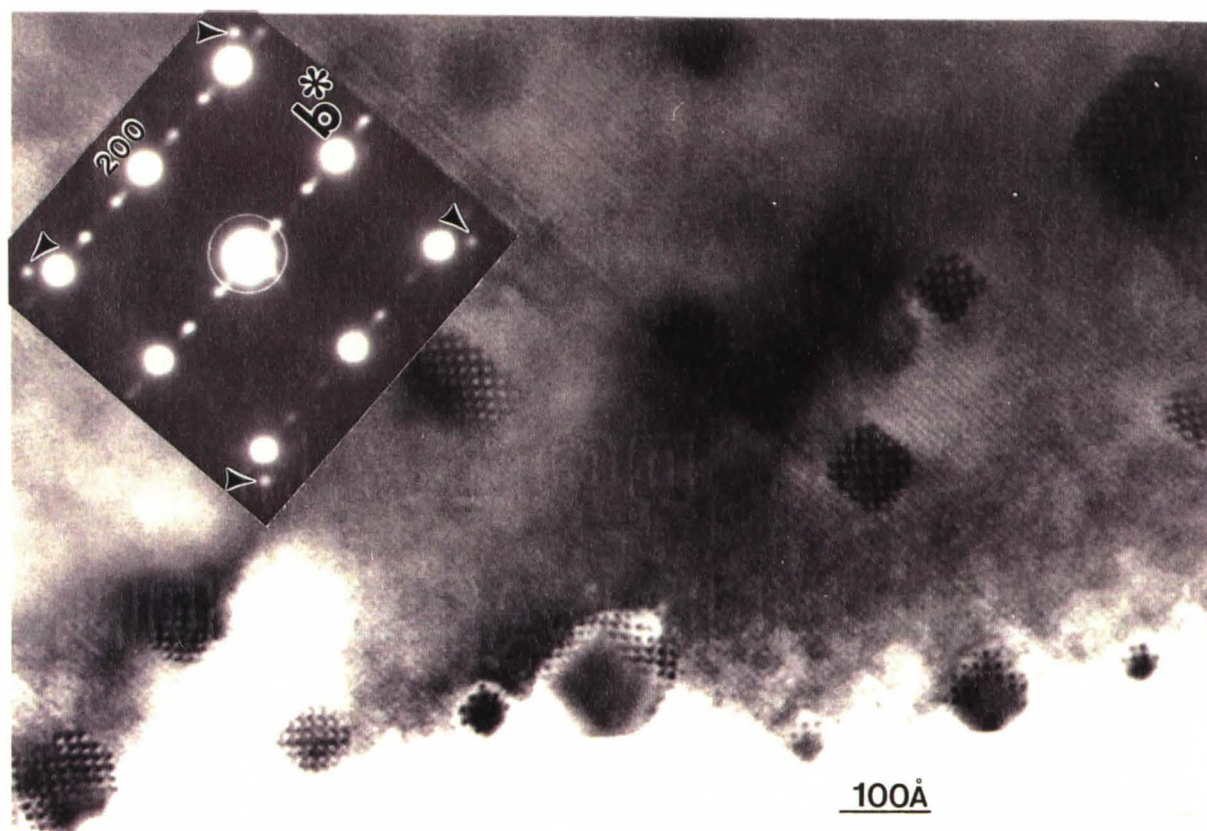


Fig 4.3 High resolution image of a heavily irradiated spinelloid crystal viewed along the [001] zone axis. The Moiré fringes created by the formation of small crystallites on the sample surface are clearly visible. Extra reflections (indicated by arrows) in the diffraction pattern identify the crystallites as Ni metal ($d_{200} = 1.77\text{\AA}$). Weaker satellite reflections arising from double diffraction are also visible.

shows a sample with very distinct Moiré fringes arising from the crystallites formed on the sample surface by beam damage. Using the diffraction pattern of a heavily irradiated crystal, these crystallites have been identified as nickel metal.

The [100] direction was the best orientation for imaging work because of the structural relationship between the spinelloid phases. According to Hyde et al. (1982) the spinelloid phases can be described as various sequences of identical building blocks joined by anti-phase boundaries (S), and mirror twin planes (T), parallel to the (010) planes of the spinelloids (see Fig 1.3). These two types of boundaries are observed by viewing the structure along the [001] and [100] directions but, due to the shorter a -dimension ($\approx 5.8 \text{ \AA}$, c.f. Table 4.1), the [100] orientation is preferred for recording lattice images.

Most of the crystals examined were well ordered, although it was possible to observe intergrowth of various phases, especially in samples which had not completely reacted. Intergrowths of spinel and phase I, and of phases I, II, and V are shown in Figs. 4.4 and 4.5 respectively, where the phases intergrow in the ac -plane as expected from their structural relationships. Unlike the NiAl_2O_4 - Ni_2SiO_4 system where intergrowths of large domains of spinel with phase I and to some extent, phase II have been observed (Barbier 1985), the NiGa_2O_4 - Ni_2SiO_4 system shows only small scale intergrowth with narrow slabs, only a few unit-cells thick, of one phase intergrown in a matrix of another phase. This difference perhaps reflects a lower solubility of Ni_2SiO_4 olivine in the NiGa_2O_4 spinel, resulting in a larger composition difference between, for instance, spinel and phase I in the gallosilicate system. Thus intergrowths in this system would involve stronger composition gradients which are unlikely to occur in crystals synthesized under the near equilibrium conditions used here (i.e. prolonged heating or slow cooling from a melt).

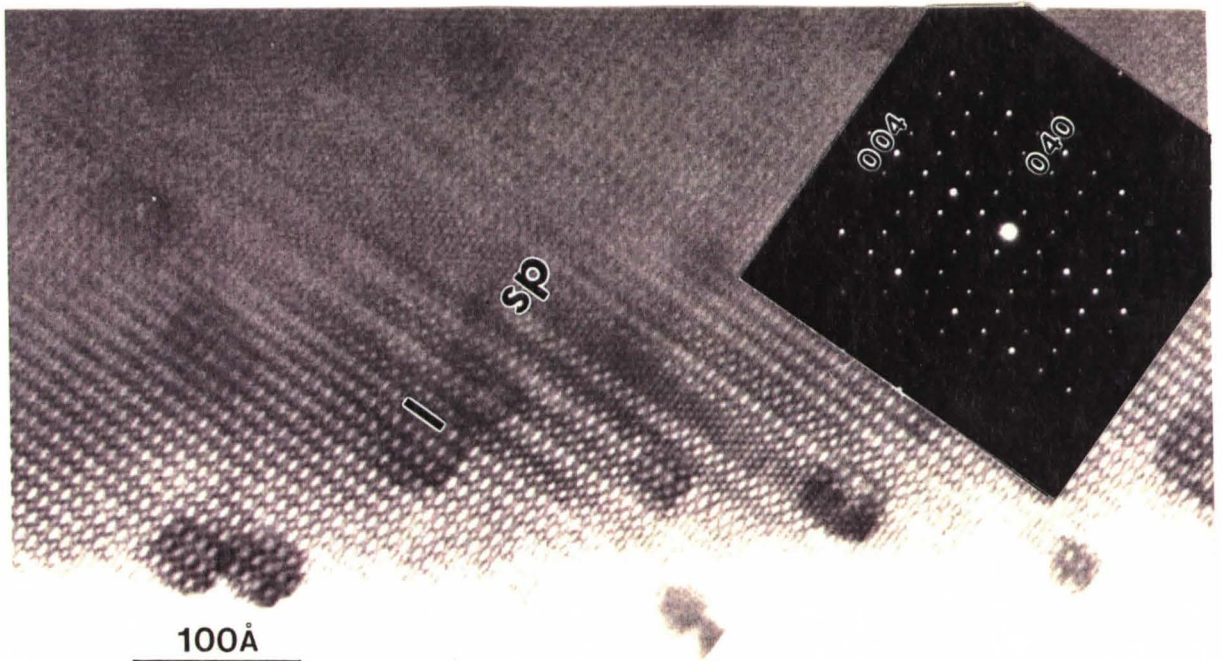


Fig. 4.4 High resolution image of nickel gallosilicate I viewed along the [100] zone axis. The image shows thin (less than 50 Å wide) regions of spinel (sp) intergrown with the phase I.

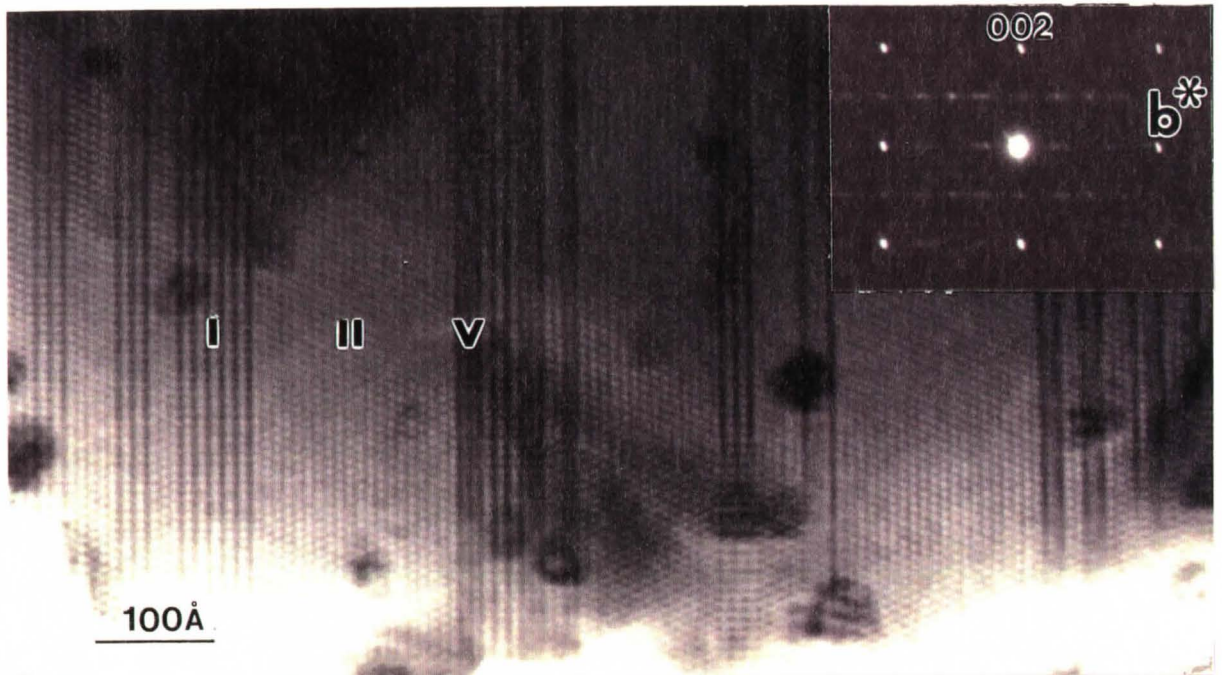


Fig. 4.5 High resolution image of a disordered nickel gallosilicate II crystal viewed along the [100] zone axis. Narrow slabs (less than 100 Å wide) of phases I and V (identified by their b -axis repeats) are intergrown with the phase II matrix

4.2 Single Crystal Results

The thermodynamic stability of all three spinelloid phases of the NiGa_2O_4 – Ni_2SiO_4 system has been confirmed by the successful growth of single crystals from a slowly cooled silica-rich melt, which is expected to produce phases with the richest possible Si content. All samples cooled from 1600°C contained some crystals of spinel, but those cooled from 1575°C showed no evidence of any spinel formation. Samples of 3 $\text{NiO} : \text{Ga}_2\text{O}_3 : \text{SiO}_2$ composition with a 30 wt% excess of SiO_2 added, produced crystals of phase V when cooled to 1540°C . However, crystals of phases I and V were obtained from similar samples cooled further (to 1525°C). This is consistent with the result of the powder experiments, namely, that phase V is the higher temperature phase. Single crystals of phase II were obtained from an Ni_2SiO_4 -rich sample of 5 $\text{NiO} : \text{Ga}_2\text{O}_3 : 2 \text{SiO}_2$ composition with a 30 wt% excess of SiO_2 which was heated to 1600°C and then cooled to 1525°C . The cooling rate (i.e. 1 or 2°C/hr) had no noticeable effect on the crystal growth.

All crystal structures were solved using direct methods. The structure solutions were complicated by the necessity to refine the occupancies of all of the cation sites. The occupancies of the octahedral sites were particularly difficult to obtain because of the inability to distinguish Ni from Ga, a result of their similar electron densities. In determining the cation occupancies it was assumed that the nickel atoms occupied only the octahedral sites and that the silicon atoms only sat at tetrahedral sites. The stoichiometry of the crystal could then be determined by refining the silicon/gallium occupancy of the tetrahedral sites and assuming that the composition could be written as $p \text{NiGa}_2\text{O}_4 : q \text{Ni}_2\text{SiO}_4$ (i.e. on the join). The octahedral cation sites were then given a uniform nickel/gallium distribution based on this stoichiometry. After a few cycles of refinement the occupancy of each octahedral site was individually estimated using the current bond lengths, the bond

valence / bond length relationship (Brown and Altermatt 1985) and equations [4.1] and [4.2]:

$$n_{Ni} V_{Ni} + n_{Ga} V_{Ga} = 2 n_{Ni} + 3 n_{Ga} \quad [4.1]$$

$$n_{Ni} + n_{Ga} = 1 \quad [4.2]$$

In these equations n_{Ni} and n_{Ga} are the cation occupancies of the site and V_{Ni} and V_{Ga} are the bond valence sums corresponding to full site occupancy by Ni and Ga respectively. The occupancies were then scaled to provide a stoichiometry consistent with the tetrahedral population. The composition was allowed to vary during a few cycles of refinement and was then kept constant during the final cycles in order to be able to refine the temperature factors.

4.2.1 Phase I

The phase I crystal was a dark green rectangular plate measuring 0.05 x 0.12 x 0.20 mm. It was found to have an orthorhombic unit cell with dimensions $a = 5.778(2)$, $b = 11.723(2)$, $c = 8.243(2)$ Å in space-group *Pmma*, slightly larger than that given by the powder data (c.f. Table 4.1), and a calculated density of 5.857 g/cm³. The unit cell contents were determined to be Ni_{10.3(2)}Ga_{11.2(2)}Si_{2.47(2)}O₃₂. Assuming the composition lies on the spinel – olivine join, this gives a composition of 2.8 NiGa₂O₄ : 1.2 Ni₂SiO₄ or Ni_{10.4}Ga_{11.2}Si_{2.4}O₃₂, which is within the error limits of the refined value. As expected from the crystal growth conditions this is on the Si-rich end of the composition range of the aluminosilicate phase, which has an idealized composition of 3 NiAl₂O₄ : Ni₂SiO₄ (Ma 1972).

The linear absorption coefficient was calculated as 11.51 mm^{-1} and $F(000) = 928$. The data was collected over one octant at 28°C and contained 2757 independent reflections. The reflections were measured by a $\theta - 2\theta$ scan over the range from $3^\circ < 2\theta \leq 70^\circ$ resulting in index ranges of $0 \leq h \leq 11$, $0 \leq k \leq 24$, and $0 \leq l \leq 16$. The cell parameters were obtained using 23 reflections over $12.9^\circ \leq 2\theta \leq 45.0^\circ$. A numerical absorption correction was made by approximating the crystal using six boundary planes, with (0 1 0) planes bounding the top and bottom of the plate, (1 0 0) planes bounding the shorter (0.12 mm) faces of the plate's side, and (0 0 1) planes bounding the longer (0.20 mm) faces. Three standard reflections, (4 0 0), (0 8 0), and (0 0 8) were checked every 100 reflections. Of the 2757 reflections measured, 1265 were treated as observed ($|F| > 6\sigma|F|$). The model was refined by full-matrix least-squares calculations minimizing $\Sigma w(F_o - F_c)^2$ using 95 parameters, which included anisotropic temperature factors (see Appendix 1). The final residual error values, using only observed reflections, were $R = 0.057$ and $wR = 0.072$. Using all data, the final residual errors were $R = 0.129$ and $wR = 0.118$. The final difference Fourier map had $\rho_{\min} = -4.10 \text{ e}/\text{\AA}^3$ and $\rho_{\max} = 4.23 \text{ e}/\text{\AA}^3$. A secondary extinction correction ($\chi = 0.0014(2)$) was applied to the data. The scattering factors for the neutral atoms were taken from the *International Tables for X-ray Crystallography*.

The final atomic coordinates, temperature factors, and cation distributions are listed in Table 4.5. The bond lengths and oxygen-metal-oxygen (O-M-O) bond angles are listed in Tables 4.6a and 4.6b respectively. The solution of the crystal structure was not trivial to obtain due to a difficulty in properly correcting for the absorption of the crystal. The inability to make this correction properly for phase I manifests itself primarily in the large errors on some oxygen coordinates and some metal - oxygen bond lengths (c.f. Tables 4.5 and 4.6a). It is also responsible for the large amounts of electron density which remain in the Fourier difference

maps and for the somewhat high values of R and wR. Attempts to solve the structure of phase I in *Pmm2*, taking the loss of the *a*-glide into account, were very unsatisfactory.

A projection on (0 0 1) of the phase I structure is shown in Fig. 4.6. Phase I is based on a distorted cubic close – packed oxygen array, with the greatest distortions occurring for those oxygen atoms lying on the twin plane (T) boundaries within the structure. The structure contains two types of tetrahedral groups, isolated TO₄ units and T₃O₁₀ chains. As shown in Fig. 4.6 each T₃O₁₀ chain contains two crystallographically distinct tetrahedral sites. There is a correlation between the average bond lengths of the three tetrahedral sites and their occupancies (see Table 4.11), corresponding to the Si – O bond being much shorter than the Ga – O bond (1.64 Å vs. 1.85 Å, Shannon 1976). There is a similar, but less obvious, correlation between the mean bond lengths of the five octahedral sites and their Ni/Ga ratios which can be ascribed to the difference in the Ni – O and Ga – O bond lengths (2.09 Å vs. 2.02 Å, Shannon 1976).

4.2.2 Phase II

The phase II crystal used for the structure determination was a dark green rod measuring 0.11 x 0.15 x 0.32 mm. It was found to have an orthorhombic unit cell in the *Imma* space–group with dimensions $a = 5.762(2)$, $b = 17.618(2)$, $c = 8.239(2)$ Å, which closely match those obtained from the powder data (c.f. Table 4.1), and has a calculated density of 5.797 g/cm³. The unit cell contents were determined to be Ni_{16.2(2)}Ga_{15.5(3)}Si_{4.3(1)}O₄₈. Again assuming that the composition lies on the spinel – olivine join, this gives a result of 3.9 NiGa₂O₄ : 2.1 Ni₂SiO₄ or Ni_{16.2}Ga_{15.6}Si_{4.2}O₄₈. This composition is again within the error limits of the refined value and is within the composition range of the corresponding aluminosilicate

phase, which has an idealized composition of $3 \text{ NiAl}_2\text{O}_4 : 2 \text{ Ni}_2\text{SiO}_4$ (Ma 1972).

The linear absorption coefficient was calculated as 11.25 mm^{-1} and $F(000) = 1380$. The data were collected over one octant at 25°C and contained 2050 independent reflections. The reflections were measured by a $\theta - 2\theta$ scan over the range from $3^\circ < 2\theta \leq 70^\circ$ resulting in index ranges of $0 \leq h \leq 11$, $0 \leq k \leq 36$, and $0 \leq l \leq 16$. The cell parameters were obtained using 20 reflections over $14.9^\circ \leq 2\theta \leq 29.9^\circ$. A semi-empirical correction for absorption was made using the psi-scan technique. Three standard reflections, (4 4 0), (0 3 11), and (3 3 0) were checked every 100 reflections. Of the 2050 reflections measured 1272 were treated as observed ($|F| > 6\sigma|F|$). The model was refined by full-matrix least-squares calculations minimizing $\Sigma w(F_o - F_c)^2$ using 71 parameters, which included anisotropic temperature factors (see Appendix 1). The final residual error values, using only observed reflections, were $R = 0.046$ and $wR = 0.061$. Using all data, the final residual errors were $R = 0.079$ and $wR = 0.082$. The final difference Fourier map had $\rho_{\min} = -5.76 \text{ e}/\text{\AA}^3$ and $\rho_{\max} = 4.05 \text{ e}/\text{\AA}^3$. A secondary extinction correction ($\chi = 0.00129(8)$) was applied to the data. The scattering factors for the neutral atoms were taken from the *International Tables for X-ray Crystallography*.

The final atomic coordinates, temperature factors, and cation distributions are listed in Table 4.7. It should be noted that the cation distribution of the M1, M2, and M3 sites were not refined independently because the occupancies were not well behaved. Bond valence calculations and comparison of the mean bond lengths showed these three sites to be similar, and so they were fixed at equal compositions. The bond lengths and oxygen-metal-oxygen (O-M-O) bond angles are listed in Tables 4.8a and 4.8b respectively.

A projection on (0 0 1) of the phase II structure is shown in Fig. 4.7. Phase II is also based on a distorted cubic close-packed oxygen array, and has the greatest distortions occurring for those oxygen atoms lying on the twin plane (T)

boundaries within the structure. The structure contains only T_3O_{10} units, resulting in only two distinct tetrahedral sites. As in phase I there is also a good correlation in the tetrahedral sites between the Si/Ga ratio and the bond lengths (see Table 4.11), again associated with the difference in the Si – O and Ga – O bond lengths.

4.2.3 Phase V

A dark green rod measuring 0.10 x 0.11 x 0.23 mm was used for the structure determination of phase V. It was found to have an orthorhombic unit cell with dimensions $a = 5.786(2)$, $b = 8.776(2)$, $c = 8.230(2)$ Å in space group *Pmma*, slightly smaller than that obtained from the powder data (c.f. Table 4.1), with a calculated density of 6.014 g/cm³. The unit cell contents were determined to be $Ni_{7.2(1)}Ga_{9.6(1)}Si_{1.20(1)}O_{24}$. This composition lies on the spinel – olivine join, corresponding to 4.8 $NiGa_2O_4$: 1.2 Ni_2SiO_4 or $Ni_{7.2}Ga_{9.6}Si_{1.2}O_{24}$. This composition is much poorer in Si than the corresponding high–pressure aluminosilicate phase, which has an idealized composition of $NiAl_2O_4$: Ni_2SiO_4 or $Ni_9Al_6Si_3O_{24}$.

The linear absorption coefficient was calculated as 12.2 mm⁻¹ and $F(000) = 708$. The data were collected over one octant at 26°C and contained 1728 independent reflections. The reflections were measured by a $\theta - 2\theta$ scan over the range from $3^\circ < 2\theta \leq 65^\circ$ resulting in index ranges of $0 \leq h \leq 11$, $0 \leq k \leq 16$, and $0 \leq l \leq 15$. The cell parameters were obtained using 26 reflections over $14.6^\circ \leq 2\theta \leq 30.5^\circ$. A semi–empirical correction for absorption was made using the psi–scan technique. Three standard reflections, (2 3 4), (3 3 1), and (1 0 5) were checked every 100 reflections. Of the 1728 reflections measured 983 were treated as observed ($|F| > 6\sigma|F|$). The model was refined by full–matrix least–squares calculations minimizing $\Sigma w(F_o - F_c)^2$ using 72 parameters, which included anisotropic temperature factors (see Appendix 1). The final residual error values, using only

observed reflections, were $R = 0.040$ and $wR = 0.060$. Using all data, the final residual errors were $R = 0.079$ and $wR = 0.080$. The final difference Fourier map had $\rho_{\min} = -2.97 \text{ e}/\text{\AA}^3$ and $\rho_{\max} = 3.23 \text{ e}/\text{\AA}^3$. A secondary extinction correction ($\chi = 0.0051(4)$) was applied to the data. The scattering factors for the neutral atoms were taken from the *International Tables for X-ray Crystallography*.

The final atomic coordinates, temperature factors, and cation distributions are listed in Table 4.9. The bond lengths and angles are listed in Tables 4.10a and 4.10b respectively.

A projection on (0 0 1) of the phase V structure is shown in Fig. 4.8. The structure contains isolated TO_4 units and T_2O_7 units. Like phases I and II, phase V is based on a distorted cubic close-packed oxygen array and has the greatest distortions occurring for those oxygen atoms lying on the twin plane (T) boundaries within the structure. As in phases I and II there is a good correlation between the tetrahedral site occupancies and mean bond lengths (see Table 4.11). The presence of such correlations in all three structures provides further support for the refined cation distributions.

Table 4.5: Atomic Coordinates and equivalent isotropic temperature displacement coefficients (U_{eq}) with cation distributions for phase I. Cation site distributions are given by $dGa + (1-d)Ni$ for octahedral (M) sites and $dGa + (1-d)Si$ for tetrahedral (T) sites.

	x	y	z	U_{eq}	d
M1	0	0	0	0.0057(3)	0.160(10)
M2	0	$1/2$	$1/2$	0.0065(3)	0.270(10)
M3	0	0.2480(1)	0	0.0060(2)	0.420(20)
M4	$1/4$	0.1247(3)	0.2728(1)	0.0056(2)	0.160(10)
M5	$1/4$	0.3755(3)	0.2486(1)	0.0061(2)	0.630(20)
T1	$1/4$	$1/2$	-0.1220(2)	0.0057(3)	0.917(2)
T2	$1/4$	0	0.6352(3)	0.0056(4)	0.366(2)
T3	$1/4$	0.2574(1)	0.6229(2)	0.0056(2)	0.741(4)
O1	$1/4$	0.1254(12)	0.1245(8)	0.0098(13)	
O2	$1/4$	0.3675(10)	0.0044(8)	0.0059(12)	
O3	$1/4$	0.1227(13)	0.5221(9)	0.0129(15)	
O4	$1/4$	0.3749(15)	0.4934(9)	0.0115(14)	
O5	-0.0149(1)	0	0.2507(1)	0.0115(18)	
O6	0.0052(1)	$1/2$	0.2539(1)	0.0157(19)	
O7	0.0129(1)	0.2526(1)	0.2476(1)	0.0038(9)	

Table 4.6a: Bond lengths (\AA) for Phase I with standard deviations

M1 - O1	4x	2.071(10)	M5 - O2	2x	2.015(7)
M1 - O5	2x	2.068(1)	M5 - O4	2x	2.018(7)
M2 - O4	4x	2.059(12)	M5 - O6	1x	2.033(3)
M2 - O6	2x	2.029(1)	M5 - O7	1x	1.989(3)
M3 - O1	2x	2.048(10)	T1 - O2	2x	1.871(11)
M3 - O2	2x	2.012(9)	T1 - O6	2x	1.832(1)
M3 - O7	2x	2.043(1)	T2 - O3	2x	1.715(13)
M4 - O1	2x	2.046(7)	T2 - O5	2x	1.652(2)
M4 - O3	2x	2.055(7)	T3 - O3	1x	1.812(13)
M4 - O5	1x	2.124(2)	T3 - O4	1x	1.778(14)
M4 - O7	1x	2.042(2)	T3 - O7	2x	1.825(1)

Table 4.6b: O-M-O Bond Angles ($^\circ$) for Phase I

O1-M1-O12x	89.5(6)	O2-M5-O62x	93.2(3)
O1-M1-O12x	90.5(6)	O2-M5-O72x	87.8(3)
O1-M1-O54x	86.1(2)	O4-M5-O62x	88.9(4)
O1-M1-O54x	93.9(2)	O4-M5-O72x	90.1(4)
O4-M2-O42x	89.2(7)	O6-M5-O61x	88.2(1)
O4-M2-O42x	90.8(7)	O6-M5-O72x	92.3(1)
O4-M2-O64x	87.9(2)	O7-M5-O71x	87.1(1)
O4-M2-O64x	92.1(2)	O2-T1-O2 1x	112.3(6)
O1-M3-O11x	90.8(6)	O2-T1-O6 4x	109.3(1)
O1-M3-O22x	88.9(4)	O6-T1-O6 1x	107.2(1)
O1-M3-O72x	83.9(2)	O3-T2-O3 1x	114.1(7)
O1-M3-O72x	98.2(2)	O3-T2-O5 4x	108.0(2)
O2-M3-O21x	91.8(5)	O5-T2-O5 1x	110.6(2)
O2-M3-O72x	86.4(2)	O3-T3-O4 1x	111.4(5)
O2-M3-O72x	91.5(2)	O3-T3-O7 2x	104.1(2)
O1-M4-O52x	85.3(3)	O4-T3-O7 2x	112.0(2)
O1-M4-O72x	84.0(3)	O7-T3-O7 1x	112.6(1)
O3-M4-O72x	96.3(3)		
O3-M4-O52x	94.5(3)		
O5-M4-O5 1x	92.2(1)		
O5-M4-O72x	90.7(1)		
O7-M4-O7 1x	84.3(1)		

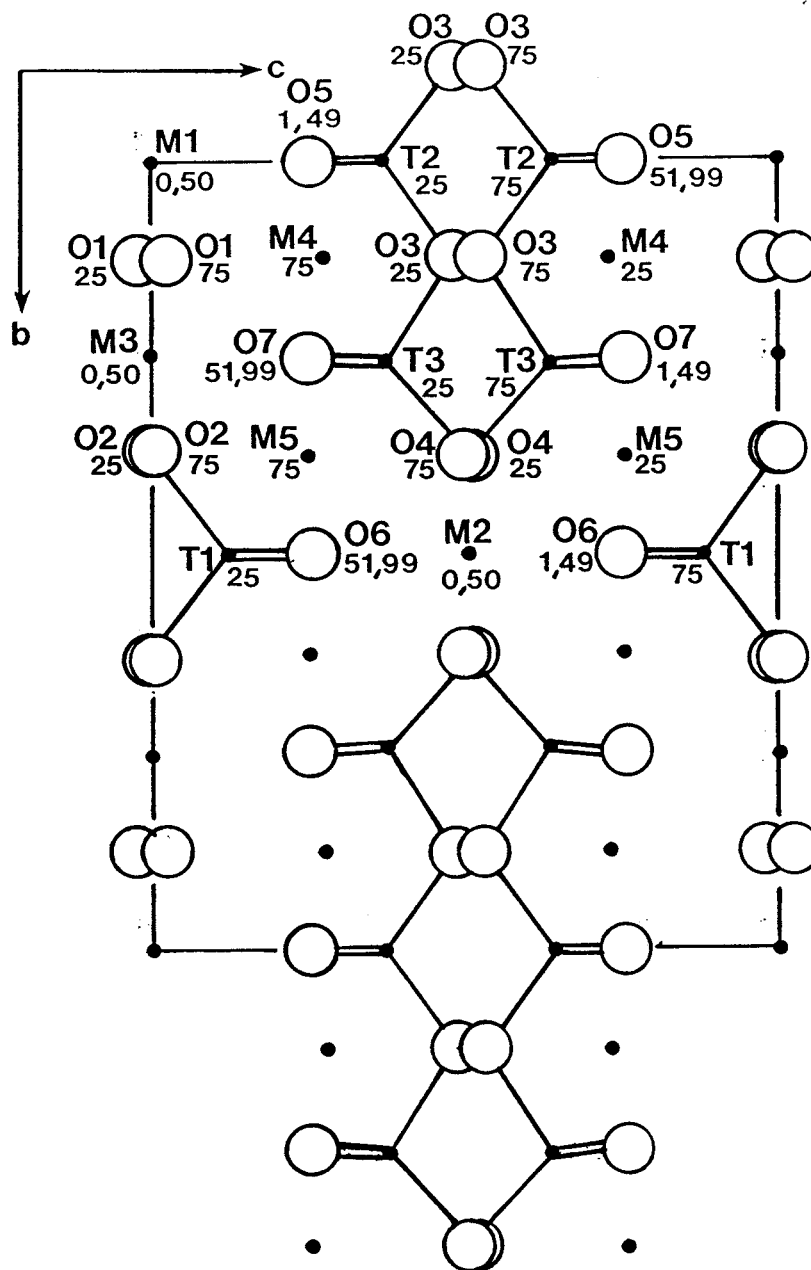


Fig. 4.6 Crystal structure of phase I projected on (100)

Table 4.7: Atomic coordinates and equivalent isotropic temperature displacement coefficients (U_{eq}) with cation distributions for phase II. Cation site distributions are given by $dGa + (1-d)Ni$ for octahedral (M) sites and $dGa + (1-d)Si$ for tetrahedral (T) sites.

	x	y	z	U_{eq}	d
M1	$1/4$	$1/4$	$3/4$	0.0036(2)	0.243(7)
M2	$1/4$	0.0851(1)	$3/4$	0.0039(1)	0.243(12)
M3	0	0.1668(1)	0.0221(1)	0.0039(1)	0.243(12)
M4	0	0	0	0.0039(2)	0.732(7)
T1	0	0.4215(1)	0.3786(1)	0.0037(1)	0.782(2)
T2	0	$1/4$	0.3846(2)	0.0036(2)	0.356(1)
O1	0	0.8319(2)	0.2270(5)	0.0069(7)	
O2	0	-0.0032(3)	0.2450(5)	0.0098(9)	
O3	0	0.1697(3)	0.2702(5)	0.0100(8)	
O4	0.2516(8)	$1/4$	0.0020(5)	0.0076(9)	
O5	0.2411(5)	0.0818(1)	0.9979(4)	0.0072(6)	

Table 4.8a: Bond lengths (\AA) for Phase II with standard deviations

M1 - O1	4x	2.048(3)	M4 - O2	2x	2.020(4)
M1 - O4	2x	2.076(4)	M4 - O5	4x	2.002(3)
M2 - O1	2x	2.061(3)	T1 - O2	1x	1.812(5)
M2 - O2	2x	2.039(4)	T1 - O3	1x	1.839(5)
M2 - O5	2x	2.044(3)	T1 - O5	2x	1.807(3)
M3 - O1	2x	2.052(4)	T2 - O3	2x	1.699(5)
M3 - O3	2x	2.045(4)	T2 - O4	2x	1.709(5)
M3 - O4	1x	2.069(3)			
M3 - O5	1x	2.052(3)			

Table 4.8b: O-M-O Bond Angles ($^\circ$) for Phase II

O1-M1-O12x	89.6(2)	O2-M4-O54x	88.4(1)
O1-M1-O12x	90.4(2)	O2-M4-O54x	91.6(1)
O1-M1-O44x	84.9(1)	O5-M4-O52x	87.9(2)
O1-M1-O44x	95.1(1)	O5-M4-O52x	92.1(2)
O1-M2-O11x	89.6(2)	O2-T1-O3 1x	113.6(2)
O1-M2-O22x	90.4(1)	O2-T1-O5 2x	111.6(1)
O1-M2-O52x	84.9(1)	O3-T1-O5 2x	104.2(1)
O1-M2-O52x	97.4(1)	O5-T1-O5 1x	111.6(1)
O2-M2-O21x	89.0(2)	O3-T2-O3 1x	112.6(3)
O2-M2-O52x	92.0(1)	O3-T2-O4 4x	107.6(1)
O2-M2-O52x	85.2(2)	O4-T2-O4 1x	113.8(3)
O1-M3-O42x	85.0(1)		
O1-M3-O52x	84.9(1)		
O3-M3-O42x	93.5(2)		
O3-M3-O52x	96.7(1)		
O4-M3-O41x	89.0(2)		
O4-M3-O52x	92.0(1)		
O5-M3-O51x	85.2(2)		

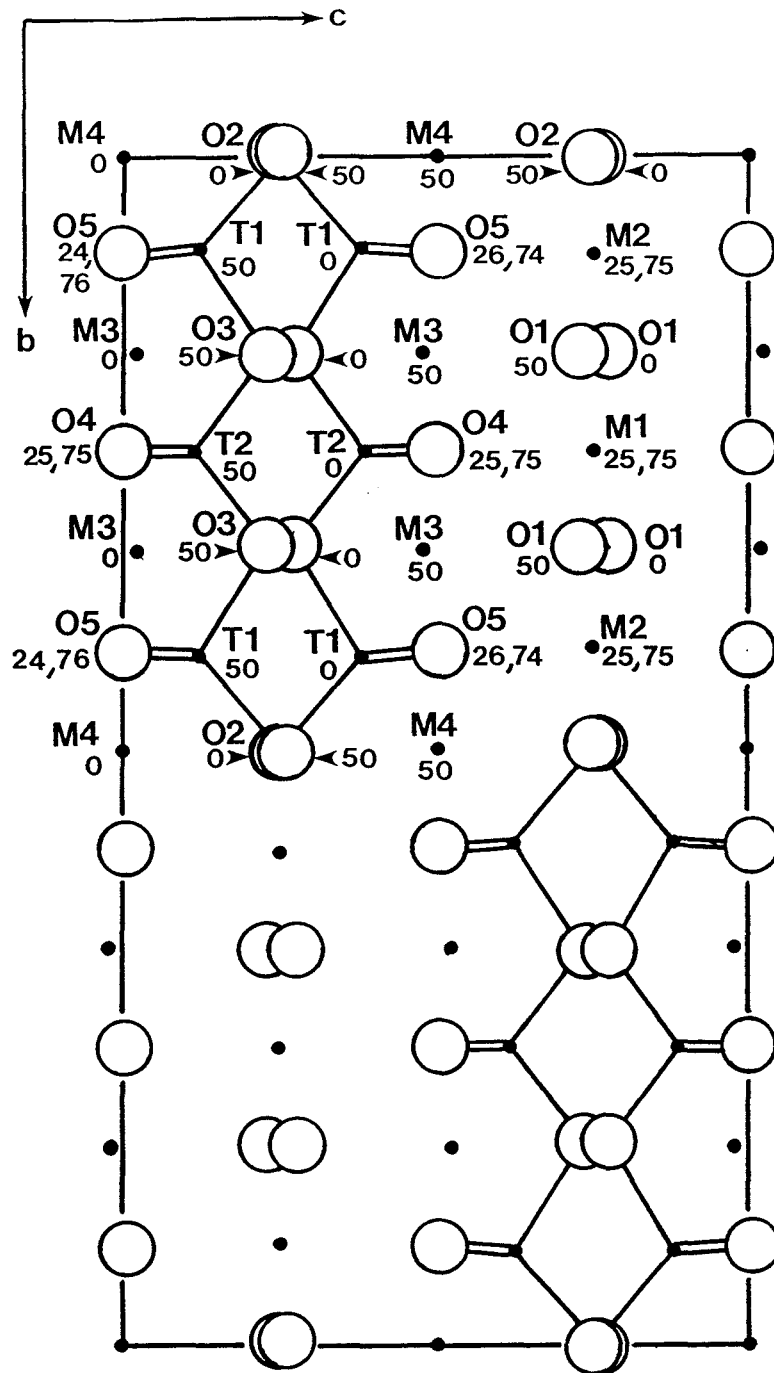


Fig. 4.7 Crystal structure of phase II projected on (100)

Table 4.9: Atomic Coordinates and equivalent isotropic temperature displacement coefficients (U_{eq}) with cation distributions for phase V. Cation site distributions are given by $d\text{Ga} + (1-d)\text{Ni}$ for octahedral (M) sites and $d\text{Ga} + (1-d)\text{Si}$ for tetrahedral (T) sites.

	x	y	z	U_{eq}	d
M1	$3/4$	0.01662(2)	0.2509(1)	0.0052(2)	0.615(13)
M2	$1/2$	0	0	0.0064(2)	0.424(8)
M3	$1/2$	0.3342(1)	$1/2$	0.0048(2)	0.322(11)
M4	$3/4$	$1/2$	0.2258(2)	0.0050(3)	0.307(8)
T1	$1/4$	0	0.3767(1)	0.0058(2)	0.949(2)
T2	$1/4$	0.3246(1)	0.1292(1)	0.0059(2)	0.726(3)
O1	0.5076(13)	0	0.2464(6)	0.0074(13)	
O2	$1/4$	0.1631(9)	0.0016(7)	0.0124(12)	
O3	$1/4$	0.1742(6)	0.5049(6)	0.0085(12)	
O4	0.5082(10)	0.3313(5)	0.2514(4)	0.0102(10)	
O5	$1/4$	$1/2$	0.0163(10)	0.0092(16)	
O6	$1/4$	$1/2$	0.5238(8)	0.0052(14)	

Table 4.10a: Bond lengths (Å) for Phase V with standard deviations

M1 - O1	2x	2.024(5)	M4 - O2	2x	2.015(7)
M1 - O2	1x	2.052(6)	M4 - O4	2x	2.018(7)
M1 - O3	1x	2.011(5)	M4 - O6	1x	2.033(3)
M1 - O4	2x	2.015(5)	M4 - O7	1x	1.989(3)
M2 - O1	2x	2.028(5)	T1 - O1	2x	1.836(7)
M2 - O2	4x	2.035(6)	T1 - O3	2x	1.858(5)
M3 - O3	2x	2.016(4)	T2 - O2	1x	1.779(7)
M3 - O5	2x	2.047(3)	T2 - O4	2x	1.802(5)
M3 - O6	2x	2.061(1)	T2 - O5	1x	1.789(4)

Table 4.10b: O-M-O Bond Angles (°) for Phase V

O1-M1-O11x	87.8(3)	O4-M4-O42x	92.6(3)
O1-M1-O22x	88.4(2)	O4-M4-O42x	86.2(3)
O1-M1-O32x	92.5(2)	O4-M4-O54x	95.9(1)
O1-M1-O42x	92.1(2)	O4-M4-O64x	84.1(1)
O2-M1-O42x	90.7(2)		
O3-M1-O42x	88.4(2)	O1-T1-O1 1x	108.5(4)
O4-M1-O41x	88.0(3)	O1-T1-O3 4x	109.4(1)
		O3-T1-O3 1x	110.8(3)
O1-M2-O24x	88.8(2)		
O1-M2-O24x	91.2(2)	O2-T2-O4 2x	111.3(2)
O2-M2-O22x	89.4(3)	O2-T2-O5 1x	112.0(3)
		O4-T2-O5 2x	105.1(2)
O3-M3-O31x	91.7(2)		
O3-M3-O32x	91.6(2)		
O3-M3-O42x	87.4(2)		
O3-M3-O62x	89.2(1)		
O4-M3-O62x	96.9(2)		
O4-M3-O62x	84.1(2)		
O6-M3-O61x	90.2(1)		

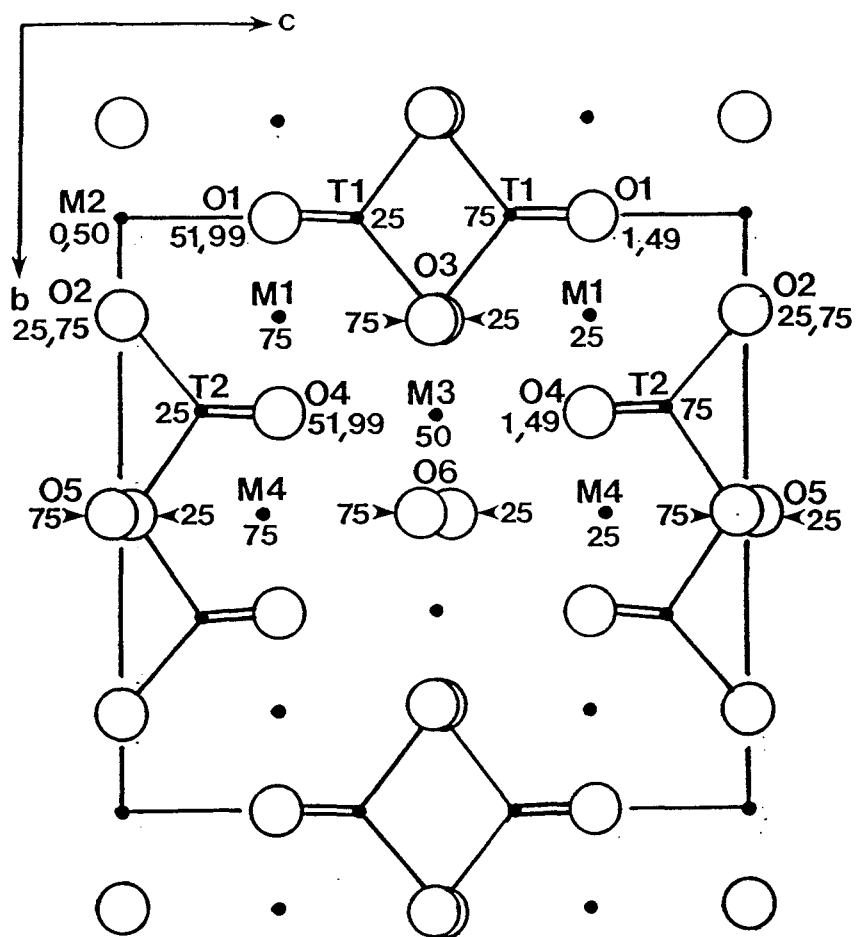


Fig. 4.8 Crystal structure of phase V projected on (100)

Table 4.11: Occupancy (as % Ga) and average bond length (Å) for the tetrahedral cation sites in the nickel gallosilicate spinelloids.

Phase	Cation Site	Occupancy	Average Bond Length
Phase I	T1	91.7	1.852
	T2	36.6	1.684
	T3	74.1	1.810
Phase II	T1	78.2	1.816
	T2	35.6	1.704
Phase V	T1	94.9	1.847
	T2	72.6	1.793

CHAPTER 5

DISCUSSION

The NiGa_2O_4 - Ni_2SiO_4 system contains three room-pressure spinelloid phases corresponding to spinelloid phases I, II, and V. Powder sample syntheses and single crystal growth indicate that phase II forms at the lowest temperatures, with phases I and V forming at increasingly higher temperatures. At very high temperatures (1575 to 1600°C) a spinel phase is also formed. Structure refinements using single crystal data indicate an increase in Ni_2SiO_4 content passing from phase V to phase I and phase II. The composition determined for phase V is unexpected since it does not follow the trend observed in the high-pressure aluminosilicate system.

All three spinelloid phases are based on a distorted cubic close-packed oxygen array, with the greatest distortions occurring around those oxygen atoms lying on the twin plane (T) boundaries within the structures. These distortions, associated with the presence of corner sharing tetrahedra, are comparable to those observed in the aluminosilicate phases. A good correlation exists in all three phases between the mean bond lengths of the tetrahedral sites and the gallium content of those sites (cf. Table 4.11). Furthermore, the observed cation distributions clearly show that there is a strong ordering of the Ga/Si atoms on the tetrahedral sites. Specifically, three types of tetrahedral site can be identified in the spinelloid structures: isolated tetrahedra (T_i), tetrahedral sites on the ends of T_2O_7 and T_3O_{10} groups (T_e), and sites in the middle of T_3O_{10} groups (T_m). Examination of the occupancies of these three types of sites shows that they are similar in all three phases: T_i with 92 to 95% Ga, T_e with 73 to 78% Ga, and T_m with 36 to 37% Ga. It is worth noting that such ordering could not be directly

determined in the aluminosilicate spinelloids because of the similarity in electron density between Si and Al. However, a similar trend in their tetrahedral occupancies is revealed by a bond valence analysis.

This specific Ga/Si ordering provides some explanation for the observed stoichiometries of the gallosilicate phases. With only isolated tetrahedral sites and T_2O_7 groups, phase V lacks the Si-rich T_m sites and, as a result, its composition is the most spinel-like. Of all the spinelloid phases it is also, in structural terms, the closest relative to spinel (with a ratio of T:S boundaries of 1:2 as opposed to 2:2 for phase I and 2:1 for phase II, see Fig 1.3). Phase I can accommodate a larger amount of Si in its structure because of the presence of the T_m sites in its T_3O_{10} groups (see Fig 1.3a). Phase II, containing T_3O_{10} groups only (see Fig 1.3b), is richest in Ni_2SiO_4 because of the ability of both the T_m and T_e sites to incorporate large amounts of Si. On the other hand, since spinel contains only isolated tetrahedra (T_i) in its structure, the maximum solubility of Ni_2SiO_4 is predicted to be about 5 to 10%. Although the structure of the spinel phase was not refined, the presence of Si in the spinel phase is revealed by the green colour of the spinel crystals obtained, as opposed to the blue colour of pure $NiGa_2O_4$ (the Si displaces the tetrahedral Ni atoms present in $NiGa_2O_4$ spinel resulting in the colour change). There is also a direct relationship between the temperature at which each phase forms and the amount of silicon in its structure.

The amount of silicon that can be incorporated into the gallosilicate spinelloids is probably limited by the large mismatch between the Ga-O and Si-O tetrahedral bond lengths (1.85 and 1.64 Å respectively - Shannon 1976). The disordering of Ga and Si atoms on the same site would cause significant distortions of the lattice due to strain. However, because the longer (and weaker) Ga-O bond is expected to be more compressible than the Si-O bond, it is possible that under pressure, the gallosilicate spinelloids may be able to incorporate more silicon on the tetrahedral sites. A dependence of composition on pressure would explain the disparate

stoichiometries of phase V in the gallosilicate and aluminosilicate systems. Unlike phases I and II, which occur at room pressure and have similar stoichiometries in both systems, the aluminosilicate phase V occurs only at very high pressure (above 7.0 GPa - Akaogi et al. 1982) and is much richer in Si than the room-pressure phase in the gallosilicate system (50% vs. 20% Ni_2SiO_4 respectively). By synthesizing the gallosilicate phase V at high pressure, it may be possible to obtain a composition closer to that observed in the aluminosilicate system because of the expected increase in the Si content. A similar argument could also explain the absence of phase V at room pressure in the aluminosilicate system. It is reasonable to assume that such a phase would be poorer in Si, similar in composition to the gallosilicate phase. However, Ni_2SiO_4 has a greater solubility range in NiAl_2O_4 (approx. 15 mol % at 1100°C, Akaogi et al. 1982) than in NiGa_2O_4 , and the spinel solid solution, instead of phase V, may therefore be expected at room pressure. A similar situation occurs in the MgGa_2O_4 - Mg_2GeO_4 system at 1 atm., where an extensive spinel solid solution includes the compositions of phase I and II (Barbier and Hyde, 1986).

Thermodynamically, the spinelloid phases are stable with respect to a mixture of spinel and olivine. Calorimetric studies of NiAl_2O_4 - Ni_2SiO_4 and MgGa_2O_4 - Mg_2GeO_4 spinelloids have found that these phases are very likely stabilized by configurational entropy (Akaogi and Navrotsky 1984, Leinenweber and Navrotsky 1989), indicating that the cation ordering/disordering may play an important role in determining phase formation in these systems. This role of entropy in stabilizing the spinelloid phases is also consistent with our observation that phase V forms at higher temperature than phase I. With fewer cation sites available in the structure of phase V, a higher temperature would be required to compensate for a smaller configurational entropy and maintain a stabilizing $-T\Delta S$ contribution to the free energy. Similarly, the spinel structure, with only one tetrahedral site, will be stabilized at even higher temperatures. Although phase II contains only two tetrahedral and four octahedral

sites, the same number as phase V, its structure allows it to accommodate more Si. As a result, phase II has a more disordered structure, possibly allowing to have a greater configurational entropy and permitting its formation at relatively lower temperature. The limitations imposed on the stoichiometry of the spinelloid phases, together with entropy considerations, help explain the absence, in the gallosilicate system, of phase III, previously observed at room pressure in the $\text{MgGa}_2\text{O}_4 - \text{Mg}_2\text{GeO}_4$ (Barbier and Hyde 1986) and $\text{MgFe}_2\text{O}_4 - \text{Mg}_2\text{GeO}_4$ (Barbier 1989) systems, and of phase IV. If these phases maintained the same degree of occupancies on their tetrahedral sites as phases I, II, and V, they would then have compositions of 2.64 $\text{NiGa}_2\text{O}_4 : \text{Ni}_2\text{SiO}_4$ for phase III and 3.35 $\text{NiGa}_2\text{O}_4 : \text{Ni}_2\text{SiO}_4$ for phase IV. Thus the unobserved phases would have compositions lying between those of phases V (4:1) and phase I (2.27:1). As mentioned above, it is not unreasonable for phase V to form because of its structural similarity to spinel and its ability to gain stability from configurational entropy. As well, phase I contains a large number of cation sites and is able to gain a large amount of configurational entropy. On the other hand, phase III, forming at an intermediate composition, would contain only one type of tetrahedral site (see Fig 1.3c) and would be therefore be unable to gain any configurational entropy from Ga/Si disordering, which possibly explains its absence in the system. Phase IV, which contains isolated tetrahedra and T_2O_7 units, also has fewer types of tetrahedral sites than phase I, and hence it too would have less entropy gain from cation disordering.

In conclusion, the discovery of three room-pressure spinelloid phases (I,II, and V) in the $\text{NiGa}_2\text{O}_4 - \text{Ni}_2\text{SiO}_4$ system provides more experimental evidence to support the suggestion that such phases are only found in spinel-olivine systems containing an inverse spinel end-member. Of the five known spinelloid structures, four of them (I, II, III, and V), have now been observed *at room pressure* in a number of such systems. This fact and the insights garnered from the structure determinations of the nickel gallosilicate spinelloids clearly indicate that, rather than pressure alone, a

combination of pressure-, composition-, and entropy-related effects determine the formation of spinelloid phases. The present study shows in particular that, under conditions of constant pressure, a close relationship exists between the chemical composition and the type of spinelloid structure formed.

REFERENCES

- Akaogi M, Akimoto S, Horioka K, Takahashi K, Horiuchi H (1982) The system $\text{NiAl}_2\text{O}_4\text{-Ni}_2\text{SiO}_4$ at high pressure and temperatures: Spinelloids with spinel-related structures. *J Solid State Chem* 44:257-267
- Akaogi M, Navrotsky A (1984) Calorimetric study of the stability of spinelloids in the system $\text{NiAl}_2\text{O}_4\text{-Ni}_2\text{SiO}_4$. *Phys Chem Minerals* 10:166-172
- Akimoto S, Fujisawa H (1966) Olivine - spinel transition in the system $\text{Mg}_2\text{SiO}_4 - \text{Fe}_2\text{SiO}_4$ at 800°C. *Earth Planet Sci Letters* 1:237-240
- Akimoto S, Fujisawa H (1968) Olivine - spinel solid solution equilibria in the system $\text{Mg}_2\text{SiO}_4 - \text{Fe}_2\text{SiO}_4$. *J Geophys Res* 73:1467-1479
- Akimoto S, Fujisawa H, Katswra T (1965) The olivine - spinel transition in Fe_2SiO_4 and Ni_2SiO_4 . *J Geophys Res* 70:1969-1977
- Akimoto S, Ida Y (1966) High pressure synthesis of Mg_2SiO_4 spinel. *Earth Planet Sci Letters* 1:358-359
- Akimoto S, Sato Y (1968) High-pressure transformation in Co_2SiO_4 olivine and some geophysical implications. *Phys Earth Planet Inter* 1:498-505

Akimoto S, Syono Y (1970) High-pressure decomposition of the system $\text{Fe}_2\text{SiO}_4 - \text{Mg}_2\text{SiO}_4$. *Phys Planet Interiors* 3:186-188

Ashcroft NW, Mermin ND (1976) Solid State Physics, New York, Montreal: Holt, Rinehart and Winston

Barbier J (1985) PhD thesis (unpublished), Australian National University

Barbier J (1989) New spinelloid phases in the MgGa_2O_4 - Mg_2GeO_4 and MgFe_2O_4 - Mg_2GeO_4 systems. *Eur J Mineral* 1:39-46

Barbier J, Hyde BG (1986) Spinelloid phases in the system MgGa_2O_4 - Mg_2GeO_4 . *Phys Chem Minerals* 13:382-392

Binns RA, Davis RJ, Reed SBJ (1969) Ringwoodite, natural $(\text{Mg,Fe})_2\text{SiO}_4$ spinel in the Tenham meteorite. *Nature* 221:943-944

Brown ID, Altermatt D (1985) Bond-valence parameters obtained from a systematic analysis of the inorganic crystal structure database. *Acta Cryst B* 41:244-247

Dachille F, Roy R (1960) High pressure studies of the system $\text{Mg}_2\text{GeO}_4 - \text{Mg}_2\text{SiO}_4$ with special reference to the olivine - spinel transition. *Am J Sci* 258:225-246

Horioka K, Nishiguchi M, Morimoto N, Horiuchi H, Akaogi M, Akimoto S (1981b) Structure of nickel aluminosilicate (phase V): A high-pressure phase related to spinel. *Acta Cryst B* 32:638-640

Horioka K, Takahashi K, Morimoto N, Horiuchi H, Akaogi M, Akimoto S (1981a) Structure of nickel aluminosilicate (phase IV): a high pressure phase related to spinel. *Acta Cryst B* 37:635-638

Hyde BG, White TJ, O'Keeffe M, Johnson AWS (1982) Structures related to those of spinel and the β -phase, and a possible mechanism for the transformation olivine \leftrightarrow spinel. *Z Kristallogr* 160:53-62

Kawai N, Endoh S, Sakata S (1966) Synthesis of Mg_2SiO_4 with spinel structure. *Proc Japan Acad* 42:626-628

Leinenweber K, Navrotsky A (1989) Thermochemistry of phases in the system $MgGa_2O_4$ - Mg_2GeO_4 . *Phys Chem Minerals* 16:497-502

Ma CB (1974) New orthorhombic phases on the join $NiAl_2O_4$ - Ni_2SiO_4 : Stability and implications to mantle mineralogy. *Contrib Mineral Petrol* 45:257-279

Ma CB, Sahl K (1975) Nickel aluminosilicate, phase III. *Acta Cryst B* 31:2142-2144

Ma CB, Tillmans E (1975) Nickel aluminosilicate, phase II. *Acta Cryst B* 31:2139-2141

Ma CB, Sahl K, Tillmans E (1975) Nickel aluminosilicate, phase I. *Acta Cryst B* 31:2137-2139

Moore PB (1970) Manganostibite: A novel cubic closed packed structure type. *Amer Mineral* 55:1489-1499

Moore PB, Smith JV (1970) Crystal structure of β -Mg₂SiO₄: crystal-chemical and geophysical implications. *Phys Earth Planet Interiors* 3:166-177

Morimoto N, Tokonami M, Watanabe M, Koto K (1974) Crystal structures of three polymorphs of Co₂SiO₄. *Am Mineral* 59:475-485

Phillips B, Hutta J J, Warshaw I (1963) Phase equilibria in the system NiO-Al₂O₃-SiO₂. *J Am Ceram Soc* 46:579-583

Price GD (1983) Polytypism and the factors determining the stability of spinelloid structures. *Phys Chem Minerals* 10:77-83

Reimer L (1984) Transmission electron microscopy, Berlin, New York: Springer - Verlag

Ringwood AE (1956) The olivine - spinel transition in the Earth's mantle. *Nature* 178:1303-1304

Ringwood AE (1962) Prediction and confirmation of the olivine - spinel transition in Ni₂SiO₄. *Geochim Cosmochim Acta* 26:457-469

Ringwood AE (1963) Olivine - spinel transformation in cobalt orthosilicate. *Nature* 198:79-80

Ringwood AE, Major A (1970) The system Mg₂SiO₄-Fe₂SiO₄ at high pressures and temperatures. *Phys Earth Planet Inter* 3:89-108

Rymer TB (1970) Electron Diffraction, London: Methuen

Shannon RD (1976) Revised effective ionic radii and systematic studies of interatomic distances in halides and chalcogenides. *Acta Cryst* A32:751-767

Stout GH, Jensen LH (1989) X-ray structure determination: a practical guide, 2 ed., New York: Wiley and Sons

Visser JW (1969) A fully automatic program for finding the unit-cell from powder data. *J Appl Crystallogr* 2:89-95

Yvon K, Jeitschko W, Parthé E (1977) Lazy Pulverix, a computer program for calculating X-ray and neutron diffraction powder patterns. *J Appl Crystallogr* 10:73-74

APPENDIX I

ANISOTROPIC TEMPERATURE FACTORS

The anisotropic temperature factors for each of the three nickel gallosilicate spinelloid phases are presented in the following tables.

Table I.1: Anisotropic displacement coefficients ($\text{\AA}^2 \times 10^4$) for phase I.

	U_{11}	U_{22}	U_{33}	U_{12}	U_{13}	U_{23}
M1	51(6)	64(5)	54(5)	0	-1(5)	0
M2	58(5)	85(5)	54(5)	0	5(4)	0
M3	62(4)	66(4)	51(4)	0	-8(3)	0
M4	59(4)	59(3)	49(3)	0	0	22(5)
M5	64(4)	59(3)	58(3)	0	0	2(3)
T1	63(5)	64(5)	45(5)	0	0	0
T2	51(8)	59(7)	57(8)	0	0	0
T3	53(4)	58(4)	58(4)	0	0	0(3)
O1	82(24)	113(22)	100(24)	0	0	-82(24)
O2	58(22)	56(21)	62(18)	0	0	54(19)
O3	90(26)	198(30)	100(25)	0	0	-75(29)
O4	74(24)	182(28)	88(22)	0	0	-69(28)
O5	100(37)	83(28)	160(28)	0	-20(22)	0
O6	217(41)	103(28)	151(27)	0	26(23)	0
O7	31(16)	55(17)	28(14)	-21(13)	-7(11)	1(9)

Table I.2: Anisotropic displacement coefficients ($\text{\AA}^2 \times 10^4$) for phase II.

	U_{11}	U_{22}	U_{33}	U_{12}	U_{13}	U_{23}
M1	16	46(3)	45(2)	0	3(2)	0
M2	19	54(2)	45(2)	0	6(2)	0
M3	21	49(2)	47(2)	0	0	0(2)
M4	16	51(3)	50(2)	0	0	5(2)
T1	15	50(2)	45(2)	0	0	0(2)
T2	15	46(4)	46(4)	0	0	0
O1	27	94(13)	84(11)	0	0	-4(10)
O2	50	152(17)	90(11)	0	0	31(11)
O3	50	176(17)	74(12)	0	0	9(11)
O4	84	72(13)	71(10)	0	-13(12)	0
O5	66(12)	70(10)	82(8)	-5(9)	14(9)	0(6)

Table I.3: Anisotropic displacement coefficients ($\text{\AA}^2 \times 10^4$) for phase V.

	U_{11}	U_{22}	U_{33}	U_{12}	U_{13}	U_{23}
M1	46(4)	49(3)	61(3)	0	0	-5(2)
M2	52(5)	75(5)	65(3)	0	-10(3)	0
M3	39(3)	49(3)	56(3)	0	8(2)	0
M4	52(6)	53(5)	44(3)	0	0	0
T1	53(4)	56(4)	66(3)	0	0	0
T2	57(3)	59(3)	60(3)	0	0	1(3)
O1	9(26)	126(25)	85(15)	0	6(11)	0
O2	87(23)	165(23)	120(18)	0	0	48(19)
O3	86(22)	90(22)	78(16)	0	0	-6(15)
O4	158(25)	58(15)	91(11)	-16(17)	-2(10)	-6(9)
O5	51(30)	116(29)	107(25)	0	0	0
O6	23(26)	88(26)	45(20)	0	0	0

APPENDIX II

OBSERVED AND CALCULATED STRUCTURE FACTORS

The following tables contain the observed (F_o) and calculated (F_c) structure factors for the three crystals. The tables also include the standard deviation for the observed values. A negative standard deviation indicates that the reflection was treated as unobserved during the refinement.

h k l 10Fo 10Fc 10s		h k l 10Fo 10Fc 10s		h k l 10Fo 10Fc 10s		h k l 10Fo 10Fc 10s		h k l 10Fo 10Fc 10s	
1 6 11 102 -18-102	4 19 11 191 265 -62	0 8 12 701 711 15	1 25 12 387 -394 29	3 14 13 456 476 25					
3 6 11 116 38 -83	6 19 11 784 -783 22	2 8 12 610 610 16	1 0 13 901 877 14	5 14 13 495 476 26					
5 6 11 64 -64 -64	1 20 11 163 28 -63	4 8 12 657 640 18	3 0 13 833 820 15	0 15 13 447 467 23					
7 6 11 75 71 -75	3 20 11 630 49-130	6 8 12 503 503 27	5 0 13 802 761 18	2 15 13 67 -65 -67					
0 7 11 536 552 15	5 20 11 72 8 -72	1 9 12 114 -14-114	7 0 13 700 655 25	4 15 13 429 429 29					
2 7 11 858 -879 13	0 21 11 261 326 39	3 9 12 62 16 -62	0 1 13 197 209 -37	1 16 13 450 439 23					
4 7 11 484 486 19	2 21 11 188 -51 -53	5 9 12 166 -39 -70	2 1 13 928 -934 14	3 16 13 470 430 24					
6 7 11 773 -725 18	4 21 11 286 305 41	7 9 12 79 32 -79	4 1 13 177 189 -57	5 16 13 361 382 37					
8 7 11 431 372 35	1 22 11 238 187 39	0 10 12 449 475 20	6 1 13 818 -791 20	0 17 13 968 969 16					
1 8 11 86 91 -86	3 22 11 71 162 -71	2 10 12 379 395 23	1 2 13 471 484 18	2 17 13 236 193 -43					
3 8 11 132 114 -69	5 22 11 221 186 -56	4 10 12 415 427 25	3 2 13 449 442 21	4 17 13 906 902 19					
5 8 11 174 54 -58	0 23 11 1135 1181 16	6 10 12 387 328 31	5 2 13 458 436 26	1 18 13 264 -310 39					
7 8 11 186 114 -84	2 23 11 480 482 24	1 11 12 311 353 28	7 2 13 388 351 38	3 18 13 294 -289 37					
0 9 11 581 576 15	4 23 11 1053 1101 18	3 11 12 332 351 28	0 3 13 564 593 16	0 19 13 853 -874 17					
2 9 11 56 11 -56	1 24 11 375 396 27	5 11 12 297 301 37	2 3 13 60 -66 -60	2 19 13 261 144 38					
4 9 11 535 514 19	3 24 11 387 346 29	7 11 12 345 307 43	4 3 13 549 532 20	4 19 13 830 -820 20					
6 9 11 70 3 -70	0 25 11 925 -964 17	0 12 12 739 762 16	6 3 13 130 -53-130	1 20 13 68 102 -68					
8 9 11 456 408 35	2 25 11 138 75-115	2 12 12 1374-1374 14	1 4 13 349 390 25	3 20 13 71 115 -71					
1 10 11 356 358 21	1 26 11 374 374 29	4 12 12 707 693 18	3 4 13 413 385 23	0 21 13 345 -358 32					
3 10 11 292 310 29	0 27 11 221 -254 -51	6 12 12 1188-1143 18	5 4 13 336 322 32	2 21 13 70 83 -70					
5 10 11 329 326 32	0 0 12 816 838 13	1 13 12 464 -492 21	7 4 13 375 320 40	1 22 13 70 81 -70					
7 10 11 252 229 -55	2 0 12 1571-1614 16	3 13 12 489 -485 22	0 5 13 1165 1193 13	0 23 13 174 -120 -66					
0 11 11 1644 1683 16	4 0 12 775 747 16	5 13 12 429 -423 28	2 5 13 169 110 -49	0 0 14 757 -774 15					
2 11 11 513 541 18	6 0 12 1383-1301 16	7 13 12 445 -418 36	4 5 13 1097 1085 15	2 0 14 286 335 32					
4 11 11 1521 1501 16	8 0 12 590 582 31	0 14 12 62 45 -62	6 5 13 74 91 -74	4 0 14 724 -719 19					
6 11 11 412 428 31	1 1 12 482 -487 16	2 14 12 123 168-123	1 6 13 432 -465 21	6 0 14 343 316 39					
8 11 11 1250 1180 21	3 1 12 481 -477 18	4 14 12 170 39 -63	3 6 13 426 -429 22	1 1 14 601 -626 18					
1 12 11 638 642 15	5 1 12 379 -407 29	6 14 12 208 146 -67	5 6 13 395 -404 29	3 1 14 553 -590 22					
3 12 11 550 554 19	7 1 12 455 -402 30	1 15 12 62 24 -62	7 6 13 296 -336 -52	5 1 14 538 -558 26					
5 12 11 625 587 20	0 2 12 280 278 24	3 15 12 109 -2-109	0 7 13 1095-1141 13	0 2 14 298 324 30					
7 12 11 423 400 34	2 2 12 281 296 26	5 15 12 103 46-103	2 7 13 60 37 -60	2 2 14 302 301 31					
0 13 11 1441-1478 15	4 2 12 262 246 35	0 16 12 101 195-101	4 7 13 1041-1041 16	4 2 14 311 297 35					
2 13 11 159 -117 -50	6 2 12 308 243 36	2 16 12 268 282 35	6 7 13 202 34 -64	6 2 14 285 256 -48					
4 13 11 1318-1330 15	8 2 12 236 187 -68	4 16 12 105 181-105	1 8 13 260 241 31	1 3 14 371 -353 24					
6 13 11 157 -85 -98	1 3 12 178 32 -37	6 16 12 275 245 -50	3 8 13 259 247 37	3 3 14 331 -345 30					
1 14 11 460 486 19	3 3 12 151 0 -53	1 17 12 694 714 18	5 8 13 203 192 -59	5 3 14 261 -306 -48					
3 14 11 414 435 24	5 3 12 66 57 -66	3 17 12 640 673 20	7 8 13 256 213 -60	0 4 14 271 237 31					
5 14 11 449 442 26	7 3 12 77 -20 -77	5 17 12 682 645 21	0 9 13 509 -536 19	2 4 14 194 175 -48					
7 14 11 311 336 48	0 4 12 512 510 16	0 18 12 228 -185 -42	2 9 13 62 75 -62	4 4 14 273 219 38					
0 15 11 491 -489 18	2 4 12 499 520 17	2 18 12 1667 1646 16	4 9 13 504 -485 22	6 4 14 205 156 -70					
2 15 11 60 -14 -60	4 4 12 442 457 22	4 18 12 227 -171 -51	6 9 13 75 61 -75	1 5 14 130 -105 -92					
4 15 11 483 -446 22	6 4 12 448 426 27	1 19 12 636 -650 19	1 10 13 265 282 33	3 5 14 67 -92 -67					
6 15 11 76 -8 -76	8 4 12 376 362 44	3 19 12 633 -613 20	3 10 13 220 257 -46	5 5 14 72 -93 -72					
1 16 11 284 282 29	1 5 12 905 921 14	5 19 12 609 -593 24	5 10 13 270 261 44	0 6 14 844 875 15					
3 16 11 304 291 31	3 5 12 870 854 14	0 20 12 652 659 18	0 11 13 138 -188 -83	2 6 14 211 -203 -44					
5 16 11 181 226 -73	5 5 12 807 799 17	2 20 12 516 491 22	2 11 13 726 731 17	4 6 14 822 815 18					
7 16 11 255 257 -61	7 5 12 690 671 24	4 20 12 597 614 23	4 11 13 138 -172-138	6 6 14 298 -202 44					
0 17 11 608 -583 17	0 6 12 107 -136-107	1 21 12 143 12 -93	6 11 13 643 633 24	1 7 14 117 -24-117					
2 17 11 321 305 27	2 6 12 2178 2207 19	3 21 12 149 33 -91	1 12 13 771 740 16	3 7 14 67 -34 -67					
4 17 11 529 -529 22	4 6 12 169 -125 -57	0 22 12 499 501 23	3 12 13 713 697 19	5 7 14 74 -17 -74					
6 17 11 283 278 46	6 6 12 1823 1799 19	2 22 12 403 391 28	5 12 13 642 658 23	0 8 14 230 194 38					
1 18 11 61 18 -61	8 6 12 85 -100 -85	4 22 12 512 467 25	0 13 13 66 157 -66	2 8 14 298 278 31					
3 18 11 66 60 -66	1 7 12 874 -890 13	1 23 12 151 214 -93	2 13 13 917 -944 16	4 8 14 171 180 -75					
5 18 11 130 -23-130	3 7 12 829 -826 15	3 23 12 165 218 -85	4 13 13 178 145 -70	6 8 14 267 246 -53					
0 19 11 234 288 39	5 7 12 768 -776 19	0 24 12 592 615 22	6 13 13 844 -822 21	1 9 14 306 308 29					
2 19 11 886 -895 16	7 7 12 654 -652 25	2 24 12 911 -925 18	1 14 13 499 516 21	3 9 14 330 302 32					

h	k	l	10Fo	10Fc	10s	h	k	l	10Fo	10Fc	10s	h	k	l	10Fo	10Fc	10s	h	k	l	10Fo	10Fc	10s	h	k	l	10Fo	10Fc	10s
5	9	14	309	269	40	0	16	14	268	227	39	0	3	15	64	50	-64	2	9	15	408	-404	26	3	1	16	608	-555	22
0	10	14	303	288	30	2	16	14	68	64	-68	2	3	15	427	434	25	4	9	15	160	-38	-93	0	2	16	578	555	21
2	10	14	413	399	25	4	16	14	274	213	44	4	3	15	109	44	-109	1	10	15	314	259	32	2	2	16	587	568	22
4	10	14	353	266	31	1	17	14	138	-139	-122	1	4	15	400	407	26	3	10	15	200	232	-61	1	3	16	68	-22	-68
1	11	14	702	713	18	3	17	14	135	-130	-135	3	4	15	384	413	30	0	11	15	244	274	-42	3	3	16	165	-50	-87
3	11	14	688	680	19	0	18	14	656	691	20	5	4	15	387	349	33	2	11	15	443	-495	27	0	4	16	379	349	27
5	11	14	603	642	25	2	18	14	142	-185	-113	0	5	15	347	281	26	4	11	15	296	263	42	2	4	16	416	358	27
0	12	14	628	-679	19	1	19	14	72	-160	-72	2	5	15	1130	1146	15	1	12	15	210	-140	-49	1	5	16	225	171	-44
2	12	14	230	310	-46	0	20	14	69	124	-69	4	5	15	76	254	-76	3	12	15	220	-174	-55	3	5	16	176	153	-78
4	12	14	638	-640	21	1	0	15	194	-166	-50	1	6	15	180	151	-57	0	13	15	579	-624	22	0	6	16	1293	-1308	15
1	13	14	412	-401	25	3	0	15	276	-202	38	3	6	15	234	185	-46	2	13	15	209	329	-60	2	6	16	326	315	34
3	13	14	329	-376	35	5	0	15	240	-112	-51	5	6	15	76	96	-76	1	14	15	70	139	-70	1	7	16	221	-239	-52
5	13	14	424	-371	31	0	1	15	453	-484	23	0	7	15	67	-115	-67	0	15	15	165	10	-73	3	7	16	202	-218	-64
0	14	14	311	316	33	2	1	15	442	468	24	2	7	15	1040	-1079	16	2	15	15	242	329	-52	0	8	16	210	277	-57
2	14	14	103	161	-103	4	1	15	424	-456	29	4	7	15	257	-101	-45	1	16	15	247	301	-49	2	8	16	251	212	-44
4	14	14	297	295	42	1	2	15	173	201	-61	1	8	15	461	447	24	0	0	16	1236	1231	15	1	9	16	70	17	-70
1	15	14	252	-267	-43	3	2	15	200	174	-57	3	8	15	512	451	23	2	0	16	454	-432	25	0	10	16	385	422	31
3	15	14	285	-264	39	5	2	15	256	202	-49	0	9	15	66	-44	-66	1	1	16	570	-560	22	1	11	16	501	522	25

Observed and calculated structure factors for Nickel Gallosilicate Phase V

Page 7

h	k	l	10Fo	10Fc	10s	h	k	l	10Fo	10Fc	10s	h	k	l	10Fo	10Fc	10s	h	k	l	10Fo	10Fc	10s	h	k	l	10Fo	10Fc	10s
4	1	14	203	-196	21	3	3	14	42	-28	-42	3	5	14	318	308	16	2	0	15	158	-168	-28	3	2	15	221	-213	20
5	1	14	284	-261	17	4	3	14	407	394	13	0	6	14	187	169	22	3	0	15	110	-62	-40	0	3	15	43	56	-43
0	2	14	88	82	-57	0	4	14	61	99	-61	1	6	14	43	102	-43	0	1	15	101	145	-51	1	3	15	274	267	17
1	2	14	166	-151	23	1	4	14	108	-91	-38	2	6	14	295	290	16	1	1	15	159	-125	24	2	3	15	272	-283	17
2	2	14	113	-82	-34	2	4	14	43	-121	-43	3	6	14	149	-92	-28	2	1	15	260	257	16	0	4	15	101	-4	-47
3	2	14	150	135	-27	3	4	14	124	78	-33	0	7	14	205	-186	21	3	1	15	44	118	-44	1	4	15	229	238	19
4	2	14	134	68	-31	4	4	14	71	84	-71	1	7	14	207	-205	21	0	2	15	120	-49	-35	2	4	15	386	392	14
0	3	14	420	431	12	0	5	14	171	-198	25	2	7	14	167	147	26	1	2	15	227	224	19	0	5	15	86	69	-86
1	3	14	41	34	-41	1	5	14	339	-334	14	0	0	15	45	-68	-45	2	2	15	417	433	13	1	5	15	71	-135	-71
2	3	14	125	75	-31	2	5	14	210	200	21	1	0	15	42	34	-42												